

# Mechanism of the $\alpha$ -Zr to hexagonal-ZrO transformation and its impact on the corrosion performance of nuclear Zr Alloys

Junliang Liu<sup>1\*</sup>, Hongbing Yu<sup>2</sup>, Phani Karamched<sup>1</sup>, Jing Hu<sup>3</sup>, Guanze He<sup>1</sup>, Daniel Goran<sup>4</sup>, Gareth M. Hughes<sup>1</sup>, Angus J. Wilkinson<sup>1</sup>, Sergio Lozano-Perez<sup>1</sup>, Chris R.M. Grovenor<sup>1</sup>

<sup>1</sup>Department of Materials, University of Oxford, Parks Road, OX1 3PH, UK

<sup>2</sup>Department of Engineering Science, University of Oxford, Parks Road, Oxford OX1 3PJ, UK

<sup>3</sup>Argonne National Laboratory, 9700 S. Cass Avenue, Argonne, IL 60439, United States

<sup>4</sup>Bruker Nano GmbH, Am Studio 2D, 12489, Berlin, Germany

\*Corresponding author: bryanchina@hotmail.com

## Abstract

Displacive transformations have been widely reported in metals, alloys and ceramics, but rarely reported to be important in the aqueous corrosion of alloys. We report here our analysis of the formation of the hexagonal-ZrO suboxide during the aqueous corrosion of  $\alpha$ -Zr alloys and propose this to be a paraequilibrium displacive transformation with the rate controlled by oxygen diffusion. Two orientation relationships were identified between  $\alpha$ -Zr and hexagonal-ZrO,  $(0002)_{\alpha\text{-Zr}} \parallel (\bar{1}011)_{\text{h-ZrO}}$  and  $[\bar{2}110]_{\alpha\text{-Zr}} \parallel [10\bar{1}2]_{\text{h-ZrO}}$  or  $(0002)_{\alpha\text{-Zr}} \parallel (22\bar{4}\bar{1})_{\text{h-ZrO}}$  and  $[\bar{2}110]_{\alpha\text{-Zr}} \parallel [1\bar{1}01]_{\text{h-ZrO}}$ , with the first one more commonly observed. No specific orientation relationships between either hexagonal-ZrO and monoclinic-ZrO<sub>2</sub> or  $\alpha$ -Zr and monoclinic-ZrO<sub>2</sub> were identified, which suggests that the formation of often-reported bulk oxide texture during aqueous corrosion is not related directly to the texture of the metallic substrate. These results provide a guideline for understanding the mechanisms of crystallographic evolution during oxide growth on commercial zirconium alloys, and also demonstrate the capability of transmission Kikuchi diffraction to investigate orientation relationships in nano-scale materials.

**Keywords:** Zirconium alloys; Oxides; Corrosion; Crystallographic orientation; Electron backscatter diffraction (EBSD)

## Introduction

Zirconium alloys are used extensively as fuel cladding materials in modern light water reactors. Demands to increase the burnup of nuclear fuels and reduce both the number of fueling cycles and the volume of high-level radioactive nuclear waste has led to renewed interest in the design of zirconium alloys with improved corrosion resistance. The complex nanoscale oxide microstructure formed by corrosion has been found to directly affect the performance of zirconium alloys. For instance, the improved corrosion resistance demonstrated in recently developed alloys has been correlated to a larger oxide grain size, stronger crystallographic texture in the oxide and tighter crystallographic alignment of oxide grains compared to those observed on older alloys [1]. Larger oxide grains can lead to a dramatic reduction in the area of grain boundaries, thus suppressing the diffusion of corroding species [2]. The predominance of low-angle grain boundaries in highly textured oxide layers also offers only low mobility paths for diffusing species [3]. Both these effects can contribute to superior corrosion performance. A thorough understanding of texture formation in the nanoscale monoclinic-ZrO<sub>2</sub> (m-ZrO<sub>2</sub>) grains that dominate in oxides grown by aqueous corrosion on commercial Zr alloys, and especially the orientation relationships at the oxide/metal interface, is therefore critical to understanding how to control the microstructure of the oxide layer, and further improve the performance of these alloys in service.

Many groups have studied the crystallographic orientation relationships between  $\alpha$ -Zr (space group, P6<sub>3</sub>/mmc) and m-ZrO<sub>2</sub> (space group P4<sub>2</sub>/nmc) using techniques such as X-ray diffraction (XRD) [4, 5] and transmission electron microscopy (TEM) [6, 7]. These studies revealed a strong fibre texture in the m-ZrO<sub>2</sub> grown on Zr alloys during aqueous corrosion, with planes between  $(10\bar{3})_{\text{m-ZrO}_2}$  and  $(10\bar{6})_{\text{m-ZrO}_2}$  lying parallel to the sample surface. This texture is attributed to minimization of the stress associated with the metal-to-oxide transformation during oxidation [8]. X-ray diffraction techniques average over very many grains throughout the oxide, so TEM analysis has been applied to study micro-texture and grain orientations close to the  $\alpha$ -Zr/ZrO<sub>2</sub> interface. However, there is little agreement on the reported orientation relationships between  $\alpha$ -Zr and m-ZrO<sub>2</sub>. Early observations by Ploc [9] on single  $\alpha$ -Zr crystals suggested the epitaxial orientation relationships  $(100)_{\text{m-ZrO}_2} \parallel (0001)_{\alpha\text{-Zr}}$  and  $[001]_{\text{m-ZrO}_2} \parallel [11\bar{2}0]_{\alpha\text{-Zr}}$ . Lin et al. [10] reported the orientation relationship to be  $(010)_{\text{m-ZrO}_2} \parallel (0001)_{\alpha\text{-Zr}}$  on a Zr-Nb alloy, and the  $(020)_{\text{m-ZrO}_2} \parallel (10\bar{1}1)_{\alpha\text{-Zr}}$  relationship was proposed by Motta et al. [11] based on synchrotron diffraction results. Recent high-resolution transmission electron microscopy (HRTEM) observations on the oxide/metal interface in different alloys suggested several other orientation relationships; including  $(111)_{\text{m-ZrO}_2} \parallel (10\bar{1}0)_{\alpha\text{-Zr}}$  on Zircaloy-4 [7], and  $(200)_{\text{m-ZrO}_2} \parallel (10\bar{1}0)_{\alpha\text{-Zr}}$ ,  $(111)_{\text{m-ZrO}_2} \parallel (11\bar{2}0)_{\alpha\text{-Zr}}$  and  $(011)_{\text{m-ZrO}_2} \parallel (11\bar{2}0)_{\alpha\text{-Zr}}$  on ZIRLO [6]. These results suggest that instead of a unique relationship either

several orientation relationships are formed during the transformation from metal-to-oxide or that the local orientation relationships at the metal/oxide interface are not responsible for the formation of the bulk oxide texture. In addition, recent atom probe tomography (APT), energy dispersive X-ray spectroscopy (EDS) and electron energy loss spectroscopy (EELS) studies have shown that a thin intermediate suboxide layer often forms at Zr/ZrO<sub>2</sub> interface [12-17], and with this intermediate phase between the  $\alpha$ -Zr and bulk ZrO<sub>2</sub> it is necessary to take the suboxide into consideration when considering how orientation relationships are formed at the metal/oxide interface.

A recent thermodynamic modelling study shows that this ZrO suboxide phase, which is absent in the traditional Zr-O binary phase diagram [18], is actually an equilibrium phase over a narrow oxygen partial pressure window [19, 20]. This ZrO was also predicted from an ab-initio study to have a structure similar to hexagonal  $\omega$ -Zr (space group, P6/mmm,  $a=5.02$ - $5.03$  Å,  $c=3$ - $3.11$  Å [21, 22]), with a high content of oxygen [19, 20]. The thickness of h-ZrO suboxide layers has been observed to correlate well to the instantaneous oxidation rate [23], and our recent in-situ irradiation results have revealed that the h-ZrO suboxide is particularly susceptible to radiation damage [24], which may be a contributing factor to help explain the acceleration of corrosion rate of zirconium alloys observed in-service [25].

However, the mechanism by which the h-ZrO forms has not yet been explored. Extensive research has been undertaken to identify the mechanisms controlling the  $\alpha$  to  $\omega$  phase transformation in Ti and Zr [26-28] showing it to be displacive martensitic in nature [29, 30]. Similar transformations have been observed in steels [31, 32], shape memory alloys [33] and ceramics [34], but this kind of transformation has not been considered to play a role in the aqueous corrosion of alloys. To explore the nature of the transformation from  $\alpha$ -Zr to h-ZrO, it is necessary to analyze the orientation relationship between the two phases. Yu et al. [35] have reported that h-ZrO formed during the annealing of Zr TEM thin foils under high vacuum conditions at temperatures above 700°C has a specific crystallographic orientation relationship with the Zr matrix. Two orientation relationships were observed,  $(0002)_{\alpha\text{-Zr}} \parallel (\bar{1}011)_{\text{h-ZrO}}$  and  $[11\bar{2}0]_{\alpha\text{-Zr}} \parallel [01\bar{1}1]_{\text{h-ZrO}}$  or  $(0002)_{\alpha\text{-Zr}} \parallel (11\bar{2}0)_{\text{h-ZrO}}$  and  $[11\bar{2}0]_{\alpha\text{-Zr}} \parallel [0002]_{\text{h-ZrO}}$ , depending on the orientation of the  $\alpha$ -Zr grain relative to the foil normal. It is not clear whether these orientation relationships are also preferred when h-ZrO is formed at the oxide/metal interface during high pressure aqueous corrosion at the much lower temperatures experienced by nuclear Zr alloys in service.

In previous microstructural studies, both h-ZrO and ZrO<sub>2</sub> grains formed during aqueous corrosion have been reported to be very small (20-100 nm) [36-38], and it is challenging to carry out micro-texture analysis on such small grains using normal electron backscatter diffraction (EBSD) due to its limited spatial resolution [39]. XRD has been widely used in the study of texture in bulk m-ZrO<sub>2</sub>, as discussed above, but the crystallography of the h-ZrO suboxide using XRD has rarely been reported due to weak peak intensity from the thin suboxide, and overlapping diffraction peaks originating from multiphase samples [4, 40]. HRTEM has been shown to have the resolution to conduct grain-by-grain crystallographic analysis, but due to the time-consuming nature of manual TEM orientation analysis only a few grains can be analyzed, reducing the statistical significance of these observations and risking missing some of the minor orientation relationships. Automated crystal orientation mapping in the transmission electron microscope (ASTAR) offers a spatial resolution of  $\sim 1$  nm, and has been used successfully to map both phase and orientation in similar fine-grained microstructures [38], but no details of the orientation relationships across the metal/oxide interface were reported. Overlapping grains through the thickness of the sample can also cause problems when using transmission techniques on the fine-grained microstructures formed by the aqueous corrosion of zirconium alloys. Dynamical errors are always present in ASTAR analysis, and can be a major factor limiting its angular resolution [41], and the overlapping of grains will result in the formation of composite diffraction patterns which can lead to deconvolution problems during the template matching process [38]. These problems can be addressed by application of the new “on-axis” transmission Kikuchi diffraction (TKD) technique [42] recently developed to improve the spatial resolution of conventional EBSD mapping. By using an electron-transparent thin TEM foil instead of a bulk sample, the probed sample volume using a focused, transmitted electron beam is much smaller, and the EBSD detector collects the Kikuchi patterns coming directly from the bottom surface of the TEM foil [43-45], which can improve

spatial resolution without sacrificing angular resolution. Compared to the conventional 'off-axis' TKD configuration, the new 'on-axis' detector geometry, where the optical axis of the SEM intersects the centre of the phosphorous screen, allows us to acquire Kikuchi patterns directly below the sample where the signal yield is strongest and gnomonic distortions are minimised [46, 47]. This improves the acquisition speed, lateral spatial resolution and indexing rates [48, 49]. All of these features have made on-axis TKD suitable to study the crystallography of nano-scale zirconium oxides.

In this paper, we have used TKD to study oxide films formed on Zr alloys, and generated detailed information on the phase distributions, grain size and crystallographic orientations. We have focused on the specific crystallographic relationships at the metal/oxide interface that can help us understand the formation mechanisms of h-ZrO and its role during the aqueous corrosion of Zr alloys used in the nuclear industry.

## Materials and methods

Three types of zirconium alloy in the recrystallized (RXA) condition were supplied by the Westinghouse Electric Company; model Zr-0.5Nb and Zr-1Nb alloys and commercial Zircaloy-4. Samples were oxidised in an autoclave filled with pure water at 360°C and 18 MPa. Detailed sample information and corrosion data are summarized in Table 1. These samples were chose to compare a commerical Zircaloy-4 and model Zr-0.5Nb alloy at an early stage of corrosion, and a similar model Zr-1Nb alloy at a much later stage. As one of the aims of this study wass to investigate the correlation between oxide texture and the underlying substrate texture, and different Zr alloys have been reported to possess different textures, it is necessary to analyse the texture of the starting samples. Based on this texture analysis of the as-received bulk alloys, the geometric relationship between the initial samples, the preferred crystal orientation and the TEM foil geometry can be schematically shown in Fig.1.

Table 1 Summary of zirconium alloys used in this study and corrosion data of selected samples

Alloys	Composition (wt%)	Corrosion time (days)	Weight gain (mg/dm <sup>2</sup> )	Calculated oxide thickness (μm) [50]
Zr-0.5Nb tube	Zr-0.53Nb-0.04Fe	75	31.4	2.1
		105	35.9	2.4
Zircaloy-4 sheet	Zr-1.36Sn-0.21Fe-0.11Cr	61	26.1	1.7
		105	44.5	2.9
Zr-1Nb tube	Zr-0.91Nb-0.08Fe	540	79	5.4

Cross sectional transmission electron microscopy foils containing both the oxide layer and the metal matrix were prepared using FIB lift-out [51] with initial milling current of 7000-300 pA at 30 kV and further thinned to a uniform thickness of ~50 nm using low-energy beam at 2 kV and 200 pA on a Zeiss Crossbeam 540 SEM/FIB system. Because of the fine grain size in the oxide layers,the choice of sample thickness is very important for the TKD characterization. Thicker samples will result in an increase in the interaction volume and limit the transmitted electron intensity, leading to low spatial resolution, poor pattern resolution and long indexing times [52].

The TKD study was carried out on a Zeiss Merlin FEG-SEM system equipped with a Bruker e-flash high resolution EBSD detector. The off-axis TKD maps were acquired using the conventional configuration, where an EBSD camera with a vertical scintillator is used. In the on-axis configuration, an OPTIMUS™ TKD head was used, and the TEM foil was mounted with the TKD head positioned immediately beneath the sample in a transmission geometry. More information about the TKD configurations can be found in [44].

The detailed mapping parameters used are summarized in Table 2. The new on-axis TKD geometry reduces the acquisition time required for diffraction patterns of similar quality up to a factor of 50 compared with the off-axis geometry [17]. This improved performance is especially important in the characterization of

nanocrystalline materials where sample drift can be a serious problem. The crystallographic information for each phase used in identifying the phase distribution in the sample is summarized in Table 3. All the maps presented below have been further cleaned using the Channel 5 software to remove isolated pixels that have been incorrectly indexed or have no reliable solutions. Based on the crystallographic information acquired from TKD analysis, Crystal Maker® was used to reconstruct possible atomic arrangements at the metal/oxide interface.

The EELS multiple linear least squares (MLLS) fitting is an useful technique for mapping differences in acquired spectra for phases or features by reference to their spectral signatures [53]. This enables us to quickly map the distribution of the different phases, e.g. ZrO<sub>2</sub>, h-ZrO suboxide, oxygen-saturated zirconium and zirconium metal, from a large sample area at a pixel size of few nanometres. EELS zero-loss spectra used for this MLLS fitting were acquired using a JEOL ARM200F microscope (200kV, CFEG source, Cs probe corrected) equipped with a Gatan Imaging Filter (GIF), with a convergence angle of 31 mrad, a collection angle of 41 mrad, an energy dispersion of 0.05 eV/channel and a pixel size of 5 nm. MLLS fitting is carried out using the script in Digital Micrograph (DM) developed by Gatan Inc.

Table 2 Summary of TKD settings and mapping information

Number of data sets		5	4	1
Alloys		Zr-0.5Nb (75- and 105-day)	Zircaloy-4 (61- and 105-day)	Zr-1Nb (540-day)
TKD type		on-axis	on-axis	off-axis
TKD settings	Sample tilt	0°	0°	10°
	Detector tilt	1.3°	1.4°	4°
	HT (kV)	30	20	30
	Beam probe (nA)	1.5	1.5	1.2
	Working distance (mm)	4.8	4.8	7.4
	Detector distance (mm)	16.5	16.5	13
	Step size (nm)	4	5	11
	Dwell time (ms)	9.3	9.3	500
	Pattern resolution	320x240	320x240	400x300
	Area per map (µm <sup>2</sup> )	3-6	3-6	10.4
	Acquisition time per map (hrs)	< 1	< 1	12.0

Table 3 Crystal structures used for the TKD analysis.

Crystal structure	a(Å)	b(Å)	c(Å)	α(°)	β(°)	γ(°)	Ref
Hexagonal Zr	3.23	3.23	5.14	90	90	120	[54]
Hexagonal ZrO	5.31	3.2	3.2	90	90	120	[19]
Tetragonal ZrO <sub>2</sub>	3.59	3.59	5.18	90	90	90	[55]
Monoclinic ZrO <sub>2</sub>	5.17	5.23	5.34	90	99.25	90	[56]

## Results

### 1. Microstructure of the oxide films

The TKD technique allows simultaneous acquisition of both phase and local orientation information, and a typical set of TKD band contrast and phase maps are shown in Fig. 2. Thanks to the improvement of on-axis TKD acquisition efficiency, all the thinned regions of the pre-transition oxide layers on Zr-0.5Nb and Zircaloy-4 alloys were analyzed, while in the off-axis analysis of the oxide layers on Zr-1Nb alloy, only part of oxide layers (the post-transition oxide plus part of the pre-transition oxide) were mapped to reduce drift, Fig. 2(b).

### 1.1. Oxide phase distribution and grain morphology

As expected, most of the small grains in the oxide layer on these three alloys are found to be m-ZrO<sub>2</sub>, Fig. 2 (e, f, g and h). However, the grain morphology clearly differs from sample to sample. The oxide layers on Zr-0.5Nb, Fig.2 (a and b), contain more aligned columnar grains, while they tend to be more equiaxed on Zircaloy-4, Fig.2 (d). It is well known that Zr alloys exhibit cyclic corrosion kinetics where at the transition point the protectiveness of the oxide breaks down, the corrosion rate increases dramatically and a new corrosion cycle restarts [57]. Evidence for the second cycle of corrosion can be seen in the thicker oxide on the Zr-1Nb sample, Fig. 2(c). The pre-transition oxide on Zr-1Nb has a similar grain shape to that formed on Zr-0.5Nb, Fig.2 (a and b), but the columnar structure of the post-transition oxide seems to be less well developed and more equiaxed. For simplicity only a few examples of the equiaxed grains formed post-transition are highlighted by arrows, Fig. 2(c). If we define 2° misorientation as the threshold for low angle grain boundaries (LAGB), and the minimum grain area as 20 nm x 20 nm (25 pixels for Zr-0.5Nb map, 16 pixels for Zircaloy-4 map and 2 pixels for Zr-1Nb map), then an average grain size of 49 nm, 41 nm and 50 nm is measured for the m-ZrO<sub>2</sub> on the 75-day Zr-0.5Nb, 61-day Zircaloy-4 and 540-day Zr-1Nb samples respectively. On all three alloys both the width and the aspect ratio of these m-ZrO<sub>2</sub> grains increases gradually towards the oxide/metal interface, Fig. 2. These observations are similar to previous reports in the literature in which Zr-Nb alloys generally tend to form oxide grains with aligned columnar shapes [1, 17] while the oxide grains on Zr-Sn alloys (Zircaloy-4 for example) tend to be more equiaxed [38, 58].

A small volume fraction of equiaxed t-ZrO<sub>2</sub> grains are found scattered throughout the oxide layers. The average grain size and tetragonal fraction values are ~16 nm and ~1.6% for 75-day Zr-0.5Nb, ~20 nm and ~3% for 105-day Zr-0.5Nb, ~15 nm and ~2.8% for 61-day Zircaloy-4 and ~18 nm and ~2.8% for the 540-day Zr-1Nb (off-axis TKD, 11 nm step size) samples. Similar t-ZrO<sub>2</sub> volume fractions of ~3% were reported in thin TEM samples from 55 day-corroded Zircaloy-2 samples analyzed by ASTAR which has a similar spatial resolution to on-axis TKD [59]. The grain size of the tetragonal phase is similar on all three alloys, but the values of tetragonal phase fraction are significantly lower than reported by bulk measurement techniques, laboratory and synchrotron XRD for example, where analysis of oxide layers formed on similar alloys reported the tetragonal phase fraction to lie in the range 3–15% [60-63]. However, the non-destructive nature of these measurements should preserve the stress state in the oxide, while stress relaxation is expected to occur during the preparation of the thin TEM samples, which may lead to transformation of stress-stabilized tetragonal grains into the equilibrium monoclinic phase [64]. Other factors which can affect the phase fraction measured through TKD include FIB-induced phase transformations [65, 66] and the possibility of mis-indexing these very small grains.

### 1.2. Bulk oxide texture analysis

The texture component maps for the three materials are shown in Fig. 3. As discussed above, the oxide has been widely reported to have a strong fibre texture with the majority of the m-ZrO<sub>2</sub> grains with directions between  $(10\bar{2})_{\text{m-ZrO}_2}$  and  $(10\bar{6})_{\text{m-ZrO}_2}$  lying parallel to the surface normal [60, 67]. The maps in Fig. 3 are colored according to the orientation deviation of grains away from the  $(10\bar{4})_{\text{m-ZrO}_2}$  ||ND fibre component. The statistical distributions of the frequency of textured oxide grains as a function of angular deviation away from the fibre component are plotted in Fig. 3(e) for these three materials. More than 50% of the indexed m-ZrO<sub>2</sub> grains are observed to have  $(10\bar{4})_{\text{m-ZrO}_2}$  lying within 30° of the surface normal, in good agreement with previous normal EBSD [37] and ASTAR [59] results. The colour in the orientation maps changes gradually with depth in the oxide, with a strong texture in the outer few microns that decreases in strength towards the oxide/metal interface. This is thought to be due to stress accumulation near the oxide/metal interface [8, 62, 63]. It should be noted that any given oxide examined represents a “snapshot” of a particular stage in the corrosion process, which means that oxide grains far away from the oxide/metal interface are a product of oxidation of metal grains which might have a different orientation to the underlying surviving metal grains. Understanding the texture relationship between metal and oxide thus necessitates micro-texture and crystalline orientation analysis near the interface regions.

The formation of the oxide texture has been proposed to be linked to preferred orientation relationships between the oxide and the  $\alpha$ -Zr substrate [7, 67, 68]. Contoured  $(10\bar{4})_{m\text{-ZrO}_2}$  pole figures (PF) and the (0002) poles of the underlying  $\alpha$ -Zr grains from the regions shown in Fig. 2 and 3 are plotted in Fig. 4. Again, the m-ZrO<sub>2</sub> fibre texture is close to the  $(10\bar{4})_{m\text{-ZrO}_2}$  normal and the grains are free to rotate around this fibre axis. Only one or two  $\alpha$ -Zr grains are included in a typical TKD map, and for the 75-day Zr-0.5Nb and 61-day Zircaloy-4 samples the orientation of these are in good agreement with texture analysis from the bulk samples, Fig 4(a and c), with the (0002) normal close to the RD in the tube sample or ND in the sheet sample. The (0002) poles of the  $\alpha$ -Zr grains in the 105-day Zr-0.5Nb and 540-day Zr-1Nb deviate more than 60° from the surface normal, and two grains with slightly different orientations can be seen in Fig. 4(b and d). No specific orientation relationships between the fine grained m-ZrO<sub>2</sub> and underlying  $\alpha$ -Zr grains can be identified from these results, hence other factors must be considered when explaining what controls the oxide texture.

## 2. Oxide/metal interface microstructure

Enlarged TKD maps showing the grain morphologies, phase distributions and the crystal orientations near the oxide/metal interface in the Zr-0.5Nb and Zr-1Nb samples are shown in Fig. 5 and 6 respectively. Pole figures of the low index planes for the  $\alpha$ -Zr substrate, h-ZrO and m-ZrO<sub>2</sub> from the corresponding O/M interface regions can be found in the supplementary data, Fig. S1 and S2. The contoured pole figures of the  $\alpha$ -Zr phase in Fig. S1(a) show the expected texture, with the (0002) basal pole of the grain in the zirconium substrate in the TEM foil aligned in the radial direction, and the  $(11\bar{2}0)_{\alpha\text{-Zr}}$  prismatic pole parallel to the tangential direction of the tube sample. Two slightly misorientated  $\alpha$ -Zr grains can be seen in Fig. 6. The pole figures of the intermediate h-ZrO suboxide layer are relatively complex, as shown in Fig. S1(b) and S2(b), even though all of these suboxide grains are in contact with the same underlying zirconium grain. As before, the bulk monoclinic oxide texture lies between  $(10\bar{2})_{m\text{-ZrO}_2}$  and  $(10\bar{6})_{m\text{-ZrO}_2}$ , Fig. S1(c) and S2(c).

The distributions of texture components in the m-ZrO<sub>2</sub> and the  $\alpha$ -Zr substrate for these two materials are plotted in Fig. 5(d) and Fig. 6(e) as a function of deviation angle between the texture component and the radial direction. In the Zr-1Nb tube sample, Fig. 6, the main (0002) texture component of the underlying  $\alpha$ -Zr substrate near the oxide/metal interface lies 80° away from the centre, so the (0002) basal pole is close to the tangential direction, while one of the  $(10\bar{1}0)_{\alpha\text{-Zr}}$  poles lies close to the radial direction. The  $(10\bar{4})_{m\text{-ZrO}_2}$  texture component of the oxide formed above this  $\alpha$ -Zr grain is lies 20°-25° away from the radial direction. In the Zr-0.5Nb sample, Fig. 5, the  $(10\bar{4})_{m\text{-ZrO}_2}$  texture component of the oxide again lies 25°-30° away from the radial direction, but in this case the (0002) texture component of the underlying substrate lies 15° - 20° away from the radial direction. Compared with the large misorientation, >60°, between the (0002) basal pole of the underlying  $\alpha$ -Zr grains in the two samples, the difference between the texture of the monoclinic oxide grains that are formed on them is relatively small. Summarising these observations, we can say that similar oxide micro-textures are formed near the oxide/metal interface in all these three alloys even though the underlying  $\alpha$ -Zr grains may have very different orientations. This reinforces the point that factors other rather than specific macroscopic orientation relationships between  $\alpha$ -Zr and m-ZrO<sub>2</sub> must be responsible for the formation of texture in the bulk oxide.

The texture of oxide layers formed on different materials is also reported elsewhere to be very similar regardless of the substrate texture [69]. Based on these observations, the formation of oxide texture may be proposed to be controlled by the stress generated by the oxidation reaction at the oxide/metal interface [57, 70] since both experimental and simulation results show that a high level of stress exists during oxidation, especially near the oxide/metal interface [62, 63]. Modelling results also indicate that the observed preferred oxide orientations occupy a smaller area at the metal/oxide interface and so reduce the compressive stress [8]. As the grains grow, they also become columnar so as to favor the growth of properly oriented grains to minimize stress accumulation.

A thin discontinuous layer of h-ZrO suboxide exists between the ZrO<sub>2</sub> and the  $\alpha$ -Zr substrate in all three samples studied here. There are 19 h-ZrO grains in the areas studied on the 75-day Zr-0.5Nb sample, 26 h-ZrO grains on the 105-day Zr-0.5Nb sample, 11 h-ZrO grains on the Zircaloy-4 and 31 on the Zr-1Nb, with average sizes ranging from 60-75 nm. The h-ZrO grains formed on the 75-day Zr-0.5Nb, 61- and 105-day Zircaloy-4, Fig. 2(a and d) and Fig. S3, all show Widmanstatten-type acicular shapes, suggesting a strong crystallographic correlation between the suboxide and underlying zirconium grains. The suboxide on the 105-day Zr-0.5Nb, right side of the map in Fig.2(b), and the 540-day Zr-1Nb alloy, Fig. 2(c) and Fig. 6, shows a smoother or plate-shaped morphology. Most of the previous APT/TEM/EELS results report Widmanstatten-type suboxides [16, 17, 23, 37, 71-76], but plate-like morphologies have been found in a few cases, Figure 3-49 in [71] and Figure 4.51 in [72] for example. The obvious questions are what controls these differences in suboxide grain morphology, what possible transformation mechanisms are involved in the transformation sequence  $\alpha$ -Zr  $\rightarrow$  h-ZrO  $\rightarrow$  ZrO<sub>2</sub>, and what is the possible impact of these different morphologies on the overall corrosion behavior? Two main orientation relationships have been reported between the Zr metal substrate and the h-ZrO suboxide (or  $\omega$ -Zr) [35, 77, 78],  $(0002)_{\alpha\text{-Zr}} \parallel (\bar{1}011)_{\text{h-ZrO}}$  or  $(0002)_{\alpha\text{-Zr}} \parallel (11\bar{2}0)_{\text{h-ZrO}}$ . From the area-averaged pole figures shown in Fig. S1 and S2 it is difficult to determine the h-ZrO/ $\alpha$ -Zr orientation relationships, and so grain-by-grain analysis has been conducted in the regions highlighted in Fig. 5 and 6. The orientation of each identified h-ZrO grain has been plotted in an individual pole figure and can then be compared with the orientation of the underlying  $\alpha$ -Zr matrix. Fig. 7 shows selected grain-by-grain orientation relationships measured between the  $\alpha$ -Zr matrix and adjacent h-ZrO grains for the Zr-0.5Nb and Zr-1Nb samples. To compare these relationships clearly, we have slightly adjusted the Euler angles in the TKD maps so that the  $(0002)_{\alpha\text{-Zr}}$  poles are distributed along the radial direction for the Zr-0.5Nb sample and the tangential direction for the Zr-1Nb sample respectively.

In Fig. 7(a, b, c, e, f and g), it can be seen that for all three alloys the  $(0002)_{\alpha\text{-Zr}}$  and one of the 6  $(\bar{1}011)_{\text{h-ZrO}}$  planes are coincident, indicating a  $(0002)_{\alpha\text{-Zr}} \parallel (\bar{1}011)_{\text{h-ZrO}}$  relationship, regardless of the orientation of the underlying  $\alpha$ -Zr grains. From the  $\langle \bar{2}110 \rangle_{\alpha\text{-Zr}}$  and  $\langle 10\bar{1}2 \rangle_{\text{h-ZrO}}$  pole figures, it can also be seen that that one of the  $\langle 10\bar{1}2 \rangle_{\text{h-ZrO}}$  directions is parallel to one of the  $\langle \bar{2}110 \rangle_{\alpha\text{-Zr}}$  directions. With this specific orientation relationship, a match between the  $(01\bar{1}0)_{\alpha\text{-Zr}} \parallel (12\bar{1}0)_{\text{h-ZrO}}$  poles can be expected, and again this can be seen in the  $(01\bar{1}0)_{\alpha\text{-Zr}}$  and  $(12\bar{1}0)_{\text{h-ZrO}}$  pole figures. The only exception is the orientation relationship in region 12 in the Zr-0.5Nb sample, where from the  $(0002)_{\alpha\text{-Zr}}$  and  $(22\bar{4}\bar{1})_{\text{h-ZrO}}$  pole figures in Fig. 7(d) it can be seen that one of the  $(22\bar{4}\bar{1})_{\text{h-ZrO}}$  planes is nearly parallel to the basal plane of the  $\alpha$ -Zr. One of the  $\langle \bar{2}110 \rangle_{\alpha\text{-Zr}}$  directions is parallel to one of the  $\langle 1\bar{1}01 \rangle_{\text{h-ZrO}}$  directions, and there is a match between the  $(01\bar{1}0)_{\alpha\text{-Zr}}$  and  $(\bar{1}2\bar{1}2)_{\text{h-ZrO}}$  poles. In order to improve the statistical significance of this study we have analysed several regions of similar size in each of the 3 alloys studied, with similar results. Although due to space limitations only six examples are shown in Fig. 7 (and another two examples in Fig. S4 in the supplementary file), we have carried out grain-by-grain analysis from more than 80 suboxide grains to identify the orientation relationships between h-ZrO and the adjacent  $\alpha$ -Zr grains.

With the observation of only these two orientation relationships, it is reasonable to infer that a strong texture is developed in the suboxide layer. TKD texture component maps for  $(10\bar{4})_{\text{m-ZrO}_2}$ ,  $(\bar{1}011)_{\text{h-ZrO}}$ , and  $(0002)_{\alpha\text{-Zr}}$  are plotted in Fig. 5(c) and 6(d), and the grains coloured according to their angular deviation from the radial direction. These maps together with the statistical distributions in Fig. 5(d) and 6(e), reveal two preferred orientation relationships,  $(0002)_{\alpha\text{-Zr}} \parallel (\bar{1}011)_{\text{h-ZrO}}$  and  $[\bar{2}110]_{\alpha\text{-Zr}} \parallel [10\bar{1}2]_{\text{h-ZrO}}$  or  $(0002)_{\alpha\text{-Zr}} \parallel (22\bar{4}\bar{1})_{\text{h-ZrO}}$  and  $[\bar{2}110]_{\alpha\text{-Zr}} \parallel [1\bar{1}01]_{\text{h-ZrO}}$ .

## Discussion

### 1. The formation mechanisms of h-ZrO suboxide

Our present results confirm that the structure of the h-ZrO phase formed in all the three materials matches the hexagonal structure in both earlier experimental observations [17, 74] and atomistic predictions [19, 20].



This structure has a sub-lattice of Zr atoms in very similar positions to those found in  $\omega$ -Zr, and oxygen atoms in interstitial positions. As a result, we have looked for phase transformations that show similar features. Extensive research has been undertaken to identify the mechanisms controlling the  $\alpha$  to  $\omega$  phase transformation in the transition metals Ti and Zr [26-28, 77, 79-84], and studying this transformation may also shed light on the formation mechanisms of h-ZrO during aqueous corrosion. The most common relationship identified between the h-ZrO grains and  $\alpha$ -Zr substrate above is  $(0002)_{\alpha\text{-Zr}} \parallel (\bar{1}011)_{\text{h-ZrO}}$  and  $[\bar{2}110]_{\alpha\text{-Zr}} \parallel [10\bar{1}2]_{\text{h-ZrO}}$  which is very close to that reported between  $\alpha$ -Zr and  $\omega$ -Zr [26, 77, 79, 84], or h-ZrO grown on thin  $\alpha$ -Zr films during annealing at 700°C in the TEM [35]. Out of the 61 suboxide grains analyzed above, only one grain showed the  $(0002)_{\alpha\text{-Zr}} \parallel (22\bar{4}\bar{1})_{\text{h-ZrO}}$  and  $[\bar{2}110]_{\alpha\text{-Zr}} \parallel [1\bar{1}01]_{\text{h-ZrO}}$  relationship. A larger angular deviation in both crystal planes and directions can be seen between this relationship and the second one reported in the literature,  $(0002)_{\alpha\text{-Zr}} \parallel (11\bar{2}0)_{\text{h-ZrO}}$  and  $[11\bar{2}0]_{\alpha\text{-Zr}} \parallel [0002]_{\text{h-ZrO}}$  [27, 35]. Direct comparison of these secondary orientation relationships reported here and that in the literature can be reflected in the distribution of corresponding poles, Fig. S5. A misorientation angle of  $\sim 17^\circ$  can be seen for both planes and directions from the relationship proposed in the literature, Fig. S5(a).

The selection of specific orientation relationships may be explained by the ab initio calculations of Trinkle et al. [27] that showed the energy barrier for the  $\alpha$  to  $\omega$  transformation with the relationship  $(0002)_{\alpha\text{-Ti}} \parallel (11\bar{2}0)_{\omega\text{-Ti}}$  is much higher than that for  $(0002)_{\alpha\text{-Ti}} \parallel (\bar{1}011)_{\omega\text{-Ti}}$ , and requires significantly more atomic shuffles [26, 27]. There is also a relatively large mismatch between the second relationship identified in the current study and  $(0002)_{\alpha\text{-Zr}/\alpha\text{-Ti}} \parallel (11\bar{2}0)_{\omega\text{-Zr}/\omega\text{-Ti}}$  reported in the literature [26, 35, 79], probably a result of higher level of accumulated stress required to trigger this less favorable transformation at the metal/oxide interface. In region 12 in Fig. 5(b) two tetragonal ZrO<sub>2</sub> grains highlighted by white arrows are only expected to be stabilised when the local stress levels are high [62, 64], and are observed immediately above the single suboxide grain with the  $(0002)_{\alpha\text{-Zr}} \parallel (22\bar{4}\bar{1})_{\text{h-ZrO}}$  relationship. This may suggest that the formation of tetragonal ZrO<sub>2</sub> grains during aqueous corrosion depends on the local strain/stress conditions, and may be controlled by the orientation relationships between the underlying suboxide and the metal substrate.

The displacive transformation from  $\alpha$ -Zr (or Ti) to  $\omega$ -Zr (or Ti) under hydrostatic pressure has been shown to be controlled by time, pressure and impurities [27, 28, 81, 83, 85], so is not a simple diffusionless martensitic transformation. This behavior is similar to paraequilibrium transformations in which the larger atoms in the substitutional sites move in a military manner (without diffusion) whereas the interstitial atoms diffuse more easily and can partition between the phases [84, 86, 87]. This kind of transformation has been widely reported in the formation of Widmanstatten ferrite in steels, a displacive mechanism whose transformation rate is mainly controlled by the diffusion of carbon [86, 87]. Recalling the special Widmanstatten-type grain morphology of the h-ZrO suboxide formed during aqueous corrosion, we infer that the phase transformation mechanisms from  $\alpha$ -Zr to  $\omega$ -Zr and  $\alpha$ -Zr to h-ZrO may share some common features, with oxygen diffusion playing a similar role as carbon in the paraequilibrium transformation, and controlling the formation of h-ZrO. The direct transformation from  $\alpha$  to  $\omega$  in both Ti and Zr requires pressures in the range 2-6 GPa [28, 78, 84, 88], although this can be significantly modified by the corrosion temperature [83, 84], residual stress levels and local strains [62, 70, 74] or alloying elements and impurities [80, 82, 84]. Compressive stresses of 2 GPa at the metal/oxide interface have been reported from both experimental measurements [62] and simulations [70], and corrosion temperatures around 300°C may decrease the pressure required to trigger the transformation.

## 2. The impact of $\alpha$ -Zr orientation on suboxide nucleation

The suboxide formed during aqueous corrosion generally has an acicular morphology, but not always as shown in Fig. 2. The different morphologies of the suboxide could be a result of different underlying  $\alpha$ -Zr orientations, as shown in Fig. 8. When the underlying  $\alpha$ -Zr grain is oriented with  $\langle 0002 \rangle_{\alpha\text{-Zr}}$  parallel to the O/M interface, the suboxide formed tends to be more equiaxed and the O/M interface to be smoother, as shown on the lefthand side of Fig. 8. In contrast, when the underlying  $\alpha$ -Zr grain is orientated with

$(0002)_{\alpha\text{-Zr}}$  parallel to the O/M interface, the suboxide generally shows an acicular shape as shown on the righthand side of Fig. 8.

In order to explain this change in the suboxide grain morphology we have analyzed the orientation of coherent or semicoherent facets at the  $\alpha\text{-Zr}/\text{h-ZrO}$  interface that could provide a barrier to growth. Preferential movement of incoherent interfaces with higher mobilities than the faceted, coherent interfaces will lead to the formation of the sawtooth-like morphology observed. In Fig. 9, we show the reconstructed atomic arrangements at the  $\alpha\text{-Zr}/\text{h-ZrO}$  interface based on the orientation information extracted from one of the sawtooth-like suboxide grains from the Zircaloy-4 TKD map. The corrosion direction is close to  $\langle 0002 \rangle_{\alpha\text{-Zr}}$ , and the suboxide growth direction is close to  $\langle 10\bar{1}4 \rangle_{\alpha\text{-Zr}}$ . The residual facets will be the slow-moving interfaces, and are semi-coherent, especially on the right hand side. The atomic planes matching at bottom of the h-ZrO needle are close to  $(0002)_{\alpha\text{-Zr}} \parallel (\bar{1}011)_{\text{h-ZrO}}$ , which is an incoherent interface, and agrees with those Trinkle proposed for  $\alpha/\omega$  interfaces [27]. The  $[2110]_{\alpha\text{-Zr}}$  direction is parallel to  $[10\bar{1}2]_{\text{h-ZrO}}$ , Fig. 9(b), and  $\sim 15.6^\circ$  away from  $[10\bar{1}1]_{\text{h-ZrO}}$  also as proposed by Trinkle [27].

When the underlying  $\alpha\text{-Zr}$  grain is orientated with  $[0002]$  parallel to the O/M interface, the suboxide shows a less faceted morphology, Fig 6 and 8. This phenomenon can also be linked to the specific interface coherency, Fig. 10, by reconstructing atomic arrangements at the h-ZrO suboxide/ $\alpha\text{-Zr}$  interface in the Zr-1Nb sample. Here the h-ZrO suboxide and  $\alpha\text{-Zr}$  grains are also oriented with  $(0002)_{\alpha\text{-Zr}} \parallel (0\bar{1}1\bar{1})_{\text{h-ZrO}}$  and  $[11\bar{2}0]_{\alpha\text{-Zr}} \parallel [01\bar{1}\bar{2}]_{\text{h-ZrO}}$ , but the interface is close to the semicoherent  $(1\bar{1}00)_{\alpha\text{-Zr}} \parallel (2\bar{1}\bar{1}0)_{\text{h-ZrO}}$  facet. The thickening of the suboxide may thus occur primarily by a ledge growth mechanism [87, 89], leading to the plate-shaped suboxide morphology seen in Fig. 6 and 8.

### 3. The effect of alloying elements and impurities on suboxide growth

The pressure required to induce the  $\alpha\text{-}\omega$  phase transition in Zr and Ti alloys has been observed to change with different types and concentrations of alloying elements or impurities [80, 82]. If the necessary space within the lattice to accommodate the lattice shear is occupied by interstitials, oxygen for example, the stress required for shear deformation is likely to increase [80]. For instance, 1.1 at.% oxygen can increase the barrier energy for the  $\alpha$  to  $\omega$  transformation by 10 meV/atom, but 3.8 at.% V can decrease the barrier energy by 3 meV/atom [82] (with the model assuming zero pressure and 0 K, the energy barrier from  $\alpha\text{-Ti}$  to  $\omega\text{-Ti}$  is modelled to be 9 meV/atom [27]). Hennig et al. [82] reported that the addition of transition metals with more d electrons such as V and Fe can decrease the energy barrier for the  $\alpha\text{-}\omega$  transformation, whereas early transition metals and simple metals such as Al and non-metallic elements such as C, N and O favour  $\alpha$ , increase the energy barrier and suppress the  $\alpha\text{-}\omega$  transformation. In commercial nuclear Zr alloys, Sn and/or Nb are the major alloying elements, with small amounts of Cr, Ni, Fe and H. Based on the discussion above, we might expect these transition metal alloying elements to decrease the barrier energy for the transition from  $\alpha\text{-Zr}$  to h-ZrO, and thus favor the formation of suboxide.

Phase-field simulations have shown that anisotropy in the interfacial energy plays an important role in determining the morphology and formation rate of Widmanstätten ferrite in Fe-C alloys [90, 91] and the  $\omega$  phase in Zr alloys [28]. Not surprisingly, the larger the anisotropy of the interfacial energy, the more acicular the product phase will be. This anisotropy in the interfacial energy can also be influenced by the presence of different types of alloying elements and impurities [92]. Here we have observed that the h-ZrO suboxide formed in Zircaloy-4 alloys with Sn as the main alloying element and small amounts of Fe and Cr tends to be more acicular than h-ZrO formed on alloys which have Nb as the main alloying element, Fig. 11. The underlying  $\alpha\text{-Zr}$  grain in these two maps has a similar orientation, and so it is reasonable to infer that different morphology of suboxide may at least in part be explained by the different major alloying element in these two materials. Both Sn and Nb are energetically more stable on substitutional sites of the hexagonal close-packed lattice of  $\alpha\text{-Zr}$  than at interstitial sites [93, 94], but Sn has a much higher solubility in  $\alpha\text{-Zr}$  at  $288^\circ\text{C}$  ( $\sim 4$  at.%) than Nb ( $\sim 0.3$  at.%) [94]. As a result, the concentration of Sn occupying substitutional sites will be higher in Zircaloy-4 (and other Sn-containing alloys) than in binary Zr-Nb alloys, and that this

may be the dominant factor controlling the anisotropy of the h-ZrO suboxide/ $\alpha$ -Zr interfacial energy, and hence the morphology of the corroding interface.

## Conclusions

The present study has made extensive use of nano-scale orientation mapping by transmission Kikuchi diffraction to study reaction mechanisms at the oxide/metal interface. A thin layer of h-ZrO suboxide is observed in all the specimens characterized, although these are not always continuous, suggesting the aqueous corrosion of zirconium usually follows the pathway:  $\text{Zr} \rightarrow \text{h-ZrO} \rightarrow \text{ZrO}_2$ . The following conclusions can be drawn from the present study:

1. Two preferred orientation relationships have been identified during the  $\alpha$ -Zr  $\rightarrow$  h-ZrO transformation,  $(0002)_{\alpha\text{-Zr}} \parallel (\bar{1}011)_{\text{h-ZrO}}$  and  $[\bar{2}110]_{\alpha\text{-Zr}} \parallel [10\bar{1}2]_{\text{h-ZrO}}$  or  $(0002)_{\alpha\text{-Zr}} \parallel (22\bar{4}\bar{1})_{\text{h-ZrO}}$  and  $[\bar{2}110]_{\alpha\text{-Zr}} \parallel [1\bar{1}01]_{\text{h-ZrO}}$ , where the first one is more commonly observed. Considering the similarities (crystal structures of parent and product phases, orientation relationships and grain growth mechanisms) with those reported in the literature for the displacive martensitic transformation from  $\alpha$ -Zr (or  $\alpha$ -Ti) to  $\omega$ -Zr (or  $\omega$ -Ti), we suggest that the formation of the h-ZrO suboxide during aqueous corrosion of these cladding tube alloys may also be a paraequilibrium displacive transformation. The formation by this mechanism of suboxide layers of very different morphologies, plate or sawtooth, can also affect the overall corrosion performance by influencing the roughness and local stress state at the oxide/metal interface.
2. A fibre texture with the  $(10\bar{4})_{\text{m-ZrO}_2}$  parallel to the metal/oxide interface is observed in the m-ZrO<sub>2</sub> phase in all three alloys studied, regardless of the underlying  $\alpha$ -Zr orientations, and no specific orientation relationship between h-ZrO and m-ZrO<sub>2</sub> or  $\alpha$ -Zr and m-ZrO<sub>2</sub> was identified. This suggests that the formation of the bulk oxide texture during aqueous corrosion is not determined solely by the substrate texture. Our results are consistent with the explanation that the preferred oxide texture is related to the minimization of stress generated at the oxide/metal interface [8].
3. The suboxide morphology can be equiaxed, plate-like or sawtooth-like depending on the underlying  $\alpha$ -Zr grain orientation. Alloying elements and impurities may also change the anisotropy of the interfacial energy, and further affect the suboxide grain morphologies. Equiaxed or plate-like grains may lead to more uniform stress distributions, and a smoother metal/suboxide interface compared with the sawtooth-like h-ZrO grains often found in Sn-containing alloys. This may be a contributing factor to the widely reported improved corrosion performance of the Sn-free binary Zr-Nb alloys under in-reactor conditions.
4. This study has also demonstrated that on-axis transmission Kikuchi diffraction can be used for microstructural and crystallographic characterisation when the samples have complex phase and orientation variations at the nano-scale, and suggests that this technique has the potential to be valuable for in-depth studies of previously difficult-to-characterise materials, including highly deformed ultrafine metals, martensitic alloys and nanocrystalline materials.

## Acknowledgements

The authors acknowledge the contribution made to this work by their collaborators from Westinghouse and the MUZIC project providing zirconium samples. EPSRC grants (EP/K040375/1 and EP/N010868/1) are acknowledged for funding the ‘South of England Analytical Electron Microscope’ and the Zeiss Crossbeam FIB/SEM used in this research. Hongbing Yu acknowledges funding from the European Research Council (ERC) under the European Union’s Horizon 2020 research and innovation programme (grant agreement No. 714697).

## References

- [1] A. Yilmazbayhan, E. Breval, A.T. Motta, R.J. Comstock, Transmission electron microscopy examination of oxide layers formed on Zr alloys, *J. Nucl. Mater.* 349(3) (2006) 265-281.
- [2] J. Godlewski, J. Gros, M. Lambertin, J. Wadier, H. Weidinger, Raman spectroscopy study of the tetragonal-to-monoclinic transition in zirconium oxide scales and determination of overall oxygen diffusion by nuclear microanalysis of O<sup>18</sup>, *Zirconium in the Nuclear Industry: 9th International Symposium*, ASTM International, 1991.
- [3] C.W. Haynes, R. Smoluchowski, Grain boundary diffusion in a body-centered cubic lattice, *Acta Metall. Mater.* 3(2) (1955) 130-134.
- [4] A. Garner, M. Preuss, P. Frankel, A method for accurate texture determination of thin oxide films by glancing-angle laboratory X-ray diffraction, *J Appl. Crystallogr.* 47(2) (2014) 575-583.
- [5] C. Roy, G. David, X-ray diffraction analyses of zirconia films on zirconium and zircaloy-2, *J. Nucl. Mater.* 37(1) (1970) 71-81.
- [6] N. Ni, D. Hudson, J. Wei, P. Wang, S. Lozano-Perez, G.D.W. Smith, J.M. Sykes, S.S. Yardley, K.L. Moore, S. Lyon, R. Cottis, M. Preuss, C.R.M. Grovenor, How the crystallography and nanoscale chemistry of the metal/oxide interface develops during the aqueous oxidation of zirconium cladding alloys, *Acta Mater.* 60(20) (2012) 7132-7149.
- [7] W. Gong, H. Zhang, Y. Qiao, H. Tian, X. Ni, Z. Li, X. Wang, Grain morphology and crystal structure of pre-transition oxides formed on Zircaloy-4, *Corros. Sci.* 74 (2013) 323-331.
- [8] H. Li, M.G. Glavicic, J.A. Szpunar, A model of texture formation in ZrO<sub>2</sub> films, *Mat. Sci. Eng. A-Struct.* 366(1) (2004) 164-174.
- [9] R.A. Ploc, Electron diffraction analysis of ZrO<sub>2</sub> on  $\alpha$ -Zr (11 $\bar{2}$ 0), *J. Nucl. Mater.* 113(1) (1983) 75-80.
- [10] Y.P. Lin, O.T. Woo, D.J. Lockwood, Texture and Phases in Oxide Films on Zr-Nb Alloys, *MRS Proceedings* 343 (2011) 487.
- [11] A. Motta, M.G. da Silva, A. Yilmazbayhan, R. Comstock, Z. Cai, B. Lai, Microstructural characterization of oxides formed on model Zr alloys using synchrotron radiation, *Zirconium in the Nuclear Industry: 15th International Symposium*, ASTM International, 2009.
- [12] S. Abolhassani, G. Bart, A. Jakob, Examination of the chemical composition of irradiated zirconium based fuel claddings at the metal/oxide interface by TEM, *J. Nucl. Mater.* 399(1) (2010) 1-12.
- [13] M. Preuss, P. Frankel, S. Lozano-Perez, D. Hudson, E. Polatidis, N. Ni, J. Wei, C. English, S. Storer, K. Chong, Studies regarding corrosion mechanisms in zirconium alloys, *Zirconium in the Nuclear Industry: 16th International Symposium*, ASTM International, 2012.
- [14] Y. Dong, A.T. Motta, E.A. Marquis, Atom probe tomography study of alloying element distributions in Zr alloys and their oxides, *J. Nucl. Mater.* 442(1-3) (2013) 270-281.
- [15] K.J. Annand, I. MacLaren, M. Gass, Utilising DualEELS to probe the nanoscale mechanisms of the corrosion of Zircaloy-4 in 350°C pressurised water, *J. Nucl. Mater.* 465 (2015) 390-399.
- [16] B. de Gabory, Y. Dong, A.T. Motta, E.A. Marquis, EELS and atom probe tomography study of the evolution of the metal/oxide interface during zirconium alloy oxidation, *J. Nucl. Mater.* 462 (2015) 304-309.
- [17] J. Hu, A. Garner, N. Ni, A. Gholinia, R.J. Nicholls, S. Lozano-Perez, P. Frankel, M. Preuss, C.R.M. Grovenor, Identifying suboxide grains at the metal-oxide interface of a corroded Zr-1.0%Nb alloy using (S)TEM, transmission-EBSD and EELS, *Micron* 69 (2015) 35-42.
- [18] J. Abriata, J. Garces, R. Versaci, The O-Zr (Oxygen-Zirconium) system, *Bulletin of Alloy Phase Diagrams* 7(2) (1986) 116-124.
- [19] B. Puchala, A. Van der Ven, Thermodynamics of the Zr-O system from first-principles calculations, *Phys. Rev. B* 88(9) (2013) 094108.

- [20] R.J. Nicholls, N. Ni, S. Lozano-Perez, A. London, D.W. McComb, P.D. Nellist, C.R.M. Grovenor, C.J. Pickard, J.R. Yates, Crystal Structure of the ZrO Phase at Zirconium/Zirconium Oxide Interfaces, *Adv. Eng. Mater.* 17(2) (2015) 211-215.
- [21] B.A. Hatt, J.A. Roberts, The  $\omega$ -phase in zirconium base alloys, *Acta Metall. Mater.* 8(8) (1960) 575-584.
- [22] G.J. Cuello, A. Fernández Guillermet, G.B. Grad, R.E. Mayer, J.R. Granada, Structural properties and stability of the bcc and omega phases in the Zr-Nb system. I. Neutron diffraction study of a quenched and aged Zr-10 wt% Nb alloy, *J. Nucl. Mater.* 218(2) (1995) 236-246.
- [23] J. Hu, B. Setiadinata, T. Aarholt, A. Garner, A. Vilalta-Clemente, J. Partezana, P. Frankel, P. Bagot, S. Lozano-Perez, A. Wilkinson, M. Preuss, M. Moody, C.R.M. Grovenor, Understanding corrosion and hydrogen pickup of zirconium fuel cladding alloys: the role of oxide microstructure, porosity, suboxides and second-phase particles, *Zirconium in the Industry: 18th International Symposium*, ASTM International, 2018.
- [24] J. Liu, G. He, J. Hu, Z. Shen, M. Kirk, M. Li, E. Ryan, P. Baldo, S. Lozano-Perez, C. Grovenor, Irradiation-induced amorphization in the zirconium suboxide on Zr-0.5Nb alloys, *J. Nucl. Mater.* 513 (2019) 226-231.
- [25] V. Bouineau, G. Bénier, D. Pêcheur, J. Thomazet, A. Ambard, M. Blat, Analysis of the Waterside Corrosion Kinetics of Zircaloy-4 Fuel Cladding in French PWRs, *Nucl. Technol.* 170(3) (2010) 444-459.
- [26] J.M. Silcock, An X-ray examination of the  $\omega$  phase in TiV, TiMo and TiCr alloys, *Acta Metall. Mater.* 6(7) (1958) 481-493.
- [27] D. Trinkle, R. Hennig, S. Srinivasan, D. Hatch, M. Jones, H. Stokes, R. Albers, J. Wilkins, New mechanism for the  $\alpha$  to  $\omega$  martensitic transformation in pure titanium, *Phys. Rev. Lett.* 91(2) (2003) 025701.
- [28] H.K. Yeddu, H. Zong, T. Lookman, Alpha – omega and omega – alpha phase transformations in zirconium under hydrostatic pressure: A 3D mesoscale study, *Acta Mater.* 102 (2016) 97-107.
- [29] K. Bhattacharya, S. Conti, G. Zanzotto, J. Zimmer, Crystal symmetry and the reversibility of martensitic transformations, *Nature* 428 (2004) 55.
- [30] Z. Nishiyama, *Martensitic transformation*, Elsevier, 2012.
- [31] A. Das, P.C. Chakraborti, S. Tarafder, H.K.D.H. Bhadeshia, Analysis of deformation induced martensitic transformation in stainless steels, *Mater. Sci. and Tech. Ser.* 27(1) (2011) 366-370.
- [32] D. Kaoumi, J. Liu, Deformation induced martensitic transformation in 304 austenitic stainless steel: In-situ vs. ex-situ transmission electron microscopy characterization, *Mat. Sci. Eng. A-Struct.* 715 (2018) 73-82.
- [33] K. Otsuka, C.M. Wayman, *Shape memory materials*, Cambridge university press, 1999.
- [34] P.M. Kelly, L.R. Francis Rose, The martensitic transformation in ceramics — its role in transformation toughening, *Prog. Mater. Sci.* 47(5) (2002) 463-557.
- [35] H. Yu, Z. Yao, F. Long, P. Saidi, M.R. Daymond, In situ transmission electron microscopy study of the thermally induced formation of  $\delta'$ -ZrO in pure Zr and Zr-based alloy, *J Appl. Crystallogr.* 50(4) (2017) 1028-1035.
- [36] S. Abolhassani, R. Restani, T. Rebac, F. Groeschel, W. Hoffelner, G. Bart, W. Goll, F. Aeschbach, TEM examinations of the metal-oxide interface of zirconium based alloys irradiated in a pressurized water reactor, *Zirconium in the Nuclear Industry: 14th International Symposium*, ASTM International, 2005.
- [37] A. Garner, J. Hu, A. Harte, P. Frankel, C. Grovenor, S. Lozano-Perez, M. Preuss, The effect of Sn concentration on oxide texture and microstructure formation in zirconium alloys, *Acta Mater.* 99 (2015) 259-272.
- [38] A. Garner, A. Gholinia, P. Frankel, M. Gass, I. MacLaren, M. Preuss, The microstructure and microtexture of zirconium oxide films studied by transmission electron backscatter diffraction and automated crystal orientation mapping with transmission electron microscopy, *Acta Mater.* 80 (2014) 159-171.

- [39] A.J. Wilkinson, T.B. Britton, Strains, planes, and EBSD in materials science, *Mater. Today* 15(9) (2012) 366-376.
- [40] D.J. Spengler, A.T. Motta, R. Bajaj, J.R. Seidensticker, Z. Cai, Characterization of Zircaloy-4 corrosion films using microbeam synchrotron radiation, *J. Nucl. Mater.* 464 (2015) 107-118.
- [41] E.F. Rauch, M. Véron, Automated crystal orientation and phase mapping in TEM, *Mater. Charact.* 98 (2014) 1-9.
- [42] R.R. Keller, R.H. Geiss, Transmission EBSD from 10 nm domains in a scanning electron microscope, *J. Microsc-Oxford* 245(3) (2012) 245-251.
- [43] S. Suzuki, Features of Transmission EBSD and its Application, *J. Microsc-Oxford* 65(9) (2013) 1254-1263.
- [44] J. Liu, S. Lozano-Perez, A.J. Wilkinson, C.R.M. Grovenor, On the depth resolution of transmission Kikuchi diffraction (TKD) analysis, *Ultramicroscopy*. (under review).
- [45] H. Yu, J. Liu, P. Karamched, A.J. Wilkinson, F. Hofmann, Mapping the full lattice strain tensor of a single dislocation by high angular resolution transmission Kikuchi diffraction (HR-TKD), *Scripta Mater.* 164 (2019) 36-41.
- [46] J.J. Fundenberger, E. Bouzy, D. Goran, J. Guyon, H. Yuan, A. Morawiec, Orientation mapping by transmission-SEM with an on-axis detector, *Ultramicroscopy* 161 (2016) 17-22.
- [47] H. Yuan, E. Brodu, C. Chen, E. Bouzy, J.J. Fundenberger, L.S. Toth, On-axis versus off-axis Transmission Kikuchi Diffraction technique: application to the characterisation of severe plastic deformation-induced ultrafine-grained microstructures, *J. Microsc-Oxford* 267(1) (2017) 70-80.
- [48] N. Wollschläger, L. Palasse, I. Häusler, K. Dirscherl, F. Oswald, S. Narbey, E. Ortel, V.D. Hodoroaba, Characterization of the inner structure of porous TiO<sub>2</sub> nanoparticle films in dye sensitive solar cells (DSSC) by focused ion beam (FIB) tomography and transmission Kikuchi diffraction (TKD) in the scanning electron microscope (SEM), *Mater. Charact.* 131 (2017) 39-48.
- [49] S.Y. Lee, H.U. Guim, D.I. Kim, Y.C. Joo, C.H. Shim, J.P. Ahn, I.S. Choi, M. Abbasi, Transmission orientation imaging of copper thin films on polyimide substrates intended for flexible electronics, *Scripta Mater.* 138 (2017) 52-56.
- [50] A. Yilmazbayhan, A.T. Motta, R.J. Comstock, G.P. Sabol, B. Lai, Z. Cai, Structure of zirconium alloy oxides formed in pure water studied with synchrotron radiation and optical microscopy: relation to corrosion rate, *J. Nucl. Mater.* 324(1) (2004) 6-22.
- [51] S. Lozano-Perez, A guide on FIB preparation of samples containing stress corrosion crack tips for TEM and atom-probe analysis, *Micron* 39(3) (2008) 320-328.
- [52] K.P. Rice, R.R. Keller, M.P. Stoykovich, Specimen-thickness effects on transmission Kikuchi patterns in the scanning electron microscope, *J. Microsc-Oxford* 254(3) (2014) 129-136.
- [53] K. J. Annand, I. MacLaren, M. Gass, Utilising DualEELS to probe the nanoscale mechanisms of the corrosion of Zircaloy-4 in 350 °C pressurised water, *J. Nucl. Mater.* 465(2015) 390-399.
- [54] A.W. Hull, Crystal structure of titanium, zirconium, cerium, thorium and osmium, *Phys. Rev.* 18(1) (1921) 88-89.
- [55] B. Bondars, G. Heidemane, J. Grabis, K. Laschke, H. Boysen, J. Schneider, F. Frey, Powder diffraction investigations of plasma sprayed zirconia, *Journal of Materials Science* 30(6) (1995) 1621-1625.
- [56] J.D. McCullough, K.N. Trueblood, The crystal structure of baddeleyite (monoclinic ZrO<sub>2</sub>), *Acta Crystallogr.* 12(7) (1959) 507-511.
- [57] A.T. Motta, A. Couet, R.J. Comstock, Corrosion of Zirconium Alloys Used for Nuclear Fuel Cladding, *Ann. Rev. Mater. Res.* 45 (2015) 311-343.

- [58] B. de Gabory, A.T. Motta, K. Wang, Transmission electron microscopy characterization of Zircaloy-4 and ZIRLO™ oxide layers, *J. Nucl. Mater.* 456 (2015) 272-280.
- [59] A. Garner, F. Baxter, P. Frankel, M. Topping, A. Harte, T. Slater, P. Tejlund, J. Romero, E. C Darby, A. Cole-Baker, M. Gass, M. Preuss, Investigating the effect of zirconium oxide microstructure on corrosion performance: a comparison between neutron, proton and non-irradiated oxides, *Zirconium in the Industry: 18th International Symposium*, ASTM International, 2018.
- [60] A. Motta, A. Yilmazbayhan, R. Comstock, J. Partezana, G. Sabol, B. Lai, Z. Cai, Microstructure and Growth Mechanism of Oxide Layers Formed on Zr Alloys Studied with Micro-Beam Synchrotron Radiation, *Zirconium in the Industry: 14th International Symposium*, ASTM International, 2005.
- [61] J. Wei, P. Frankel, E. Polatidis, M. Blat, A. Ambard, R.J. Comstock, L. Hallstadius, D. Hudson, G.D.W. Smith, C.R.M. Grovenor, M. Klaus, R.A. Cottis, S. Lyon, M. Preuss, The effect of Sn on autoclave corrosion performance and corrosion mechanisms in Zr–Sn–Nb alloys, *Acta Mater.* 61(11) (2013) 4200-4214.
- [62] E. Polatidis, P. Frankel, J. Wei, M. Klaus, R.J. Comstock, A. Ambard, S. Lyon, R.A. Cottis, M. Preuss, Residual stresses and tetragonal phase fraction characterisation of corrosion tested Zircaloy-4 using energy dispersive synchrotron X-ray diffraction, *J. Nucl. Mater.* 432(1) (2013) 102-112.
- [63] H. Swan, M.S. Blackmur, J.M. Hyde, A. Laferrere, S.R. Ortner, P.D. Styman, C. Staines, M. Gass, H. Hulme, A. Cole-Baker, P. Frankel, The measurement of stress and phase fraction distributions in pre and post-transition Zircaloy oxides using nano-beam synchrotron X-ray diffraction, *J. Nucl. Mater.* 479 (2016) 559-575.
- [64] W. Qin, C. Nam, H.L. Li, J.A. Szpunar, Tetragonal phase stability in ZrO<sub>2</sub> film formed on zirconium alloys and its effects on corrosion resistance, *Acta Mater.* 55(5) (2007) 1695-1701.
- [65] F. Baxter, A. Garner, M. Topping, H. Hulme, M. Preuss, P. Frankel, Phase stability of zirconium oxide films during focused ion beam milling, *J. Nucl. Mater.* 504 (2018) 176-180.
- [66] D. Simeone, D. Gosset, J.L. Bechade, A. Chevarier, Analysis of the monoclinic–tetragonal phase transition of zirconia under irradiation, *J. Nucl. Mater.* 300(1) (2002) 27-38.
- [67] J. Lin, H. Li, J.A. Szpunar, R. Bordoni, A.M. Olmedo, M. Villegas, A.J.G. Maroto, Analysis of zirconium oxide formed during oxidation at 623 K on Zr–2.5Nb and Zircaloy-4, *Mat. Sci. Eng. A-Struct.* 381(1) (2004) 104-112.
- [68] C. Kato, Y. Ishijima, F. Ueno, M. Yamamoto, The effect of crystal textures on the anodic oxidization of zirconium in a boiling nitric acid solution, *J. of Nucl. Sci. Technol.* 53(9) (2016) 1371-1379.
- [69] A. Garner, P. Frankel, J. Partezana, M. Preuss, The effect of substrate texture and oxidation temperature on oxide texture development in zirconium alloys, *J. Nucl. Mater.* 484 (2017) 347-356.
- [70] M. Parise, O. Sicardy, G. Cailletaud, Modelling of the mechanical behavior of the metal–oxide system during Zr alloy oxidation, *J. Nucl. Mater.* 256(1) (1998) 35-46.
- [71] J. Hu, High resolution characterisation of corrosion and hydrogen pickup of Zr-Nb cladding alloys, D.Phil thesis, University of Oxford, 2016
- [72] J. Sayers, Effect of pH on hydrogen pick-up and corrosion of Zircaloy-4, D.Phil thesis, 2017, University of Oxford, 2017.
- [73] P. Tejlund, H.O. Andrén, G. Sundell, M. Thuvander, B. Josefsson, L. Hallstadius, M. Ivermark, M. Dahlbäck, Oxidation Mechanism in Zircaloy-2—The Effect of SPP Size Distribution, *Zirconium in the Nuclear Industry: 17th International Symposium*, ASTM International, 2015.
- [74] P. Bossis, G. Lelievre, P. Barberis, X. Iltis, F. Lefebvre, Multi-scale characterization of the metal-oxide interface of zirconium alloys, *Zirconium in the Nuclear Industry: 12th International Symposium*, ASTM International, 2000.
- [75] S.B. Setiadinata, Corrosion and hydrogen pickup mechanisms of zirconium alloys, D.Phil thesis, University of Oxford, 2016.

- [76] M. Preuss, P. Frankel, S. Lozano-Perez, D. Hudson, E. Polatidis, N. Ni, J. Wei, C. English, S. Storer, K. Chong, M. Fitzpatrick, P. Wang, J. Smith, C. Grovenor, G. Smith, J. Sykes, B. Cottis, S. Lyon, L. Hallstadius, B. Comstock, A. Ambard, M. Blat-Yrieix, Studies regarding corrosion mechanisms in zirconium alloys, Zirconium in the Nuclear Industry: 16th International Symposium, ASTM International, 2011.
- [77] M. Usikov, V. Zilbershtein, The orientation relationship between the  $\alpha$ - and  $\omega$ -phases of titanium and zirconium, *Phys. Status. Solidi. A* 19(1) (1973) 53-58.
- [78] H. R. Wenk, P. Kaercher, W. Kanitpanyacharoen, E. Zepeda-Alarcon, Y. Wang, Orientation relations during the  $\alpha$ - $\omega$  phase transition of zirconium: In situ texture observations at high pressure and temperature, *Phys. Rev. Lett* 111(19) (2013) 195701.
- [79] A. Rabinkin, M. Talianker, O. Botstein, Crystallography and a model of the  $\alpha \rightarrow \omega$  phase transformation in zirconium, *Acta Metall. Mater.* 29(4) (1981) 691-698.
- [80] E. Cerreta, G.T. Gray, R.S. Hixson, P.A. Rigg, D.W. Brown, The influence of interstitial oxygen and peak pressure on the shock loading behavior of zirconium, *Acta Mater.* 53(6) (2005) 1751-1758.
- [81] L. Gao, X. Ding, T. Lookman, J. Sun, E.K.H. Salje, Metastable phase transformation and hcp- $\omega$  transformation pathways in Ti and Zr under high hydrostatic pressures, *Appl. Phys. Lett.* 109(3) (2016) 031912.
- [82] R.G. Hennig, D.R. Trinkle, J. Bouchet, S.G. Srinivasan, R.C. Albers, J.W. Wilkins, Impurities block the  $\alpha$  to  $\omega$  martensitic transformation in titanium, *Nat. Mater.* 4 (2005) 129.
- [83] M.K. Jacobsen, N. Velisavljevic, S.V. Sinogeikin, Pressure-induced kinetics of the  $\alpha$  to  $\omega$  transition in zirconium, *Journal of Applied Physics* 118(2) (2015) 025902.
- [84] S.K. Sikka, Y.K. Vohra, R. Chidambaram, Omega phase in materials, *Prog. Mater. Sci.* 27(3) (1982) 245-310.
- [85] D.R. Trinkle III, A theoretical study of the hcp to omega martensitic phase transition in titanium, D.Phil thesis, the Ohio State University, 2003.
- [86] H. Bhadeshia, Phase transformations contributing to the properties of modern steels, *B. Pol. Acad. Sci-Tech* 58(2) (2010) 255-265.
- [87] H.K. Bhadeshia, Diffusional formation of ferrite in iron and its alloys, *Prog. Mater. Sci.* 29(4) (1985) 321-386.
- [88] J. Zhang, Y. Zhao, C. Pantea, J. Qian, L.L. Daemen, P.A. Rigg, R.S. Hixson, C.W. Greeff, G.T. Gray, Y. Yang, L. Wang, Y. Wang, T. Uchida, Experimental constraints on the phase diagram of elemental zirconium, *J. Phys. Chem. Solids* 66(7) (2005) 1213-1219.
- [89] G. Spanos, R.A. Masumura, R.A. Vandermeer, M. Enomoto, The evolution and growth kinetics of precipitate plates growing by the ledge mechanism, *Acta Metall. Mater.* 42(12) (1994) 4165-4176.
- [90] A. Yamanaka, T. Takaki, Y. Tomita, Phase-field simulation of austenite to ferrite transformation and Widmanstätten ferrite formation in Fe-C alloy, *Mater. Trans.* 47(11) (2006) 2725-2731.
- [91] W. Yan, N. Xiao, Y. Chen, D. Li, Phase-field modeling of Widmanstätten ferrite formation during isothermal transformation in low carbon steels, *Comp. Mater. Sci.* 81 (2014) 503-509.
- [92] X. L. Liu, S. L. Shang, Y. J. Hu, Y. Wang, Y. Du, Z. K. Liu, Insight into  $\gamma$ -Ni/ $\gamma'$ -Ni<sub>3</sub>Al interfacial energy affected by alloying elements, *Mater. Design* 133 (2017) 39-46.
- [93] M. Christensen, T.M. Angelu, J.D. Ballard, J. Vollmer, R. Najafabadi, E. Wimmer, Effect of impurity and alloying elements on Zr grain boundary strength from first-principles computations, *J. Nucl. Mater.* 404(2) (2010) 121-127.
- [94] M. Christensen, W. Wolf, C.M. Freeman, E. Wimmer, R.B. Adamson, L. Hallstadius, P.E. Cantonwine, E.V. Mader, Effect of alloying elements on the properties of Zr and the Zr-H system, *J. Nucl. Mater.* 445(1) (2014) 241-250.





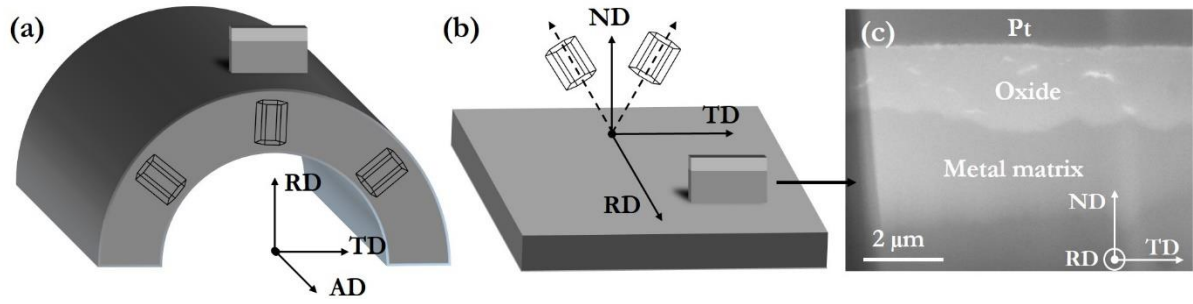


Fig. 1. 3-D schematic diagrams of the dominant crystal orientation in conventionally manufactured Zr alloys, (a) tube sample, AD: axial direction, TD: tangential direction, RD: radial direction, (b) sheet sample, RD: rolling direction, TD: transverse direction, ND: normal direction and (c) the corresponding TEM lamellar orientation (SEM view of the TEM foil from the Zircaloy-4 sheet sample).

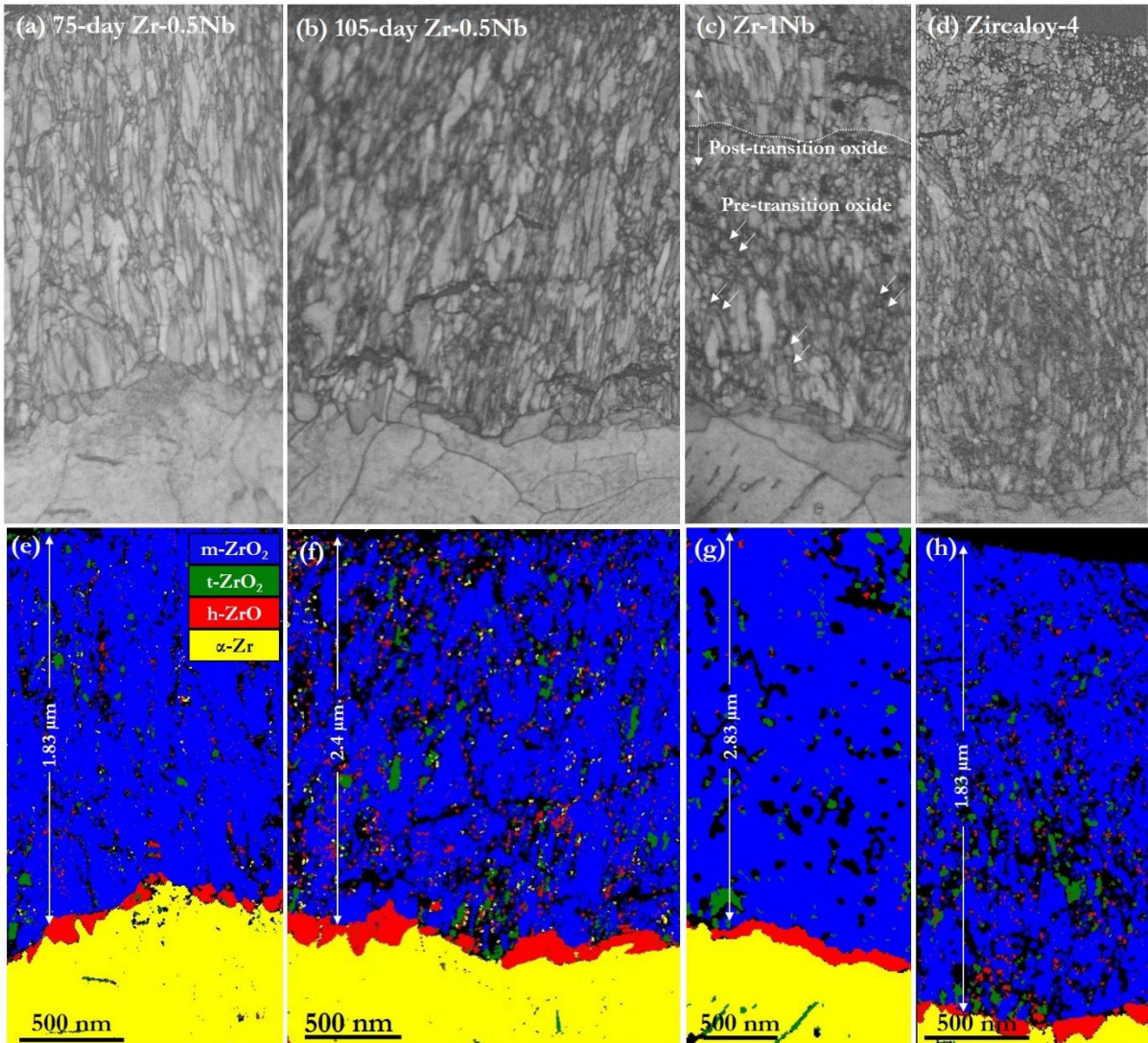


Fig. 2. TKD band contrast and phase maps from the oxide layer on (a, e) the 75-day corroded Zr-0.5Nb sample, (b, f) the 105-day corroded Zr-0.5Nb sample, (c, g) the 540-day corroded Zr-1Nb sample and (d, h) the 61-day corroded Zircaloy-4 sample

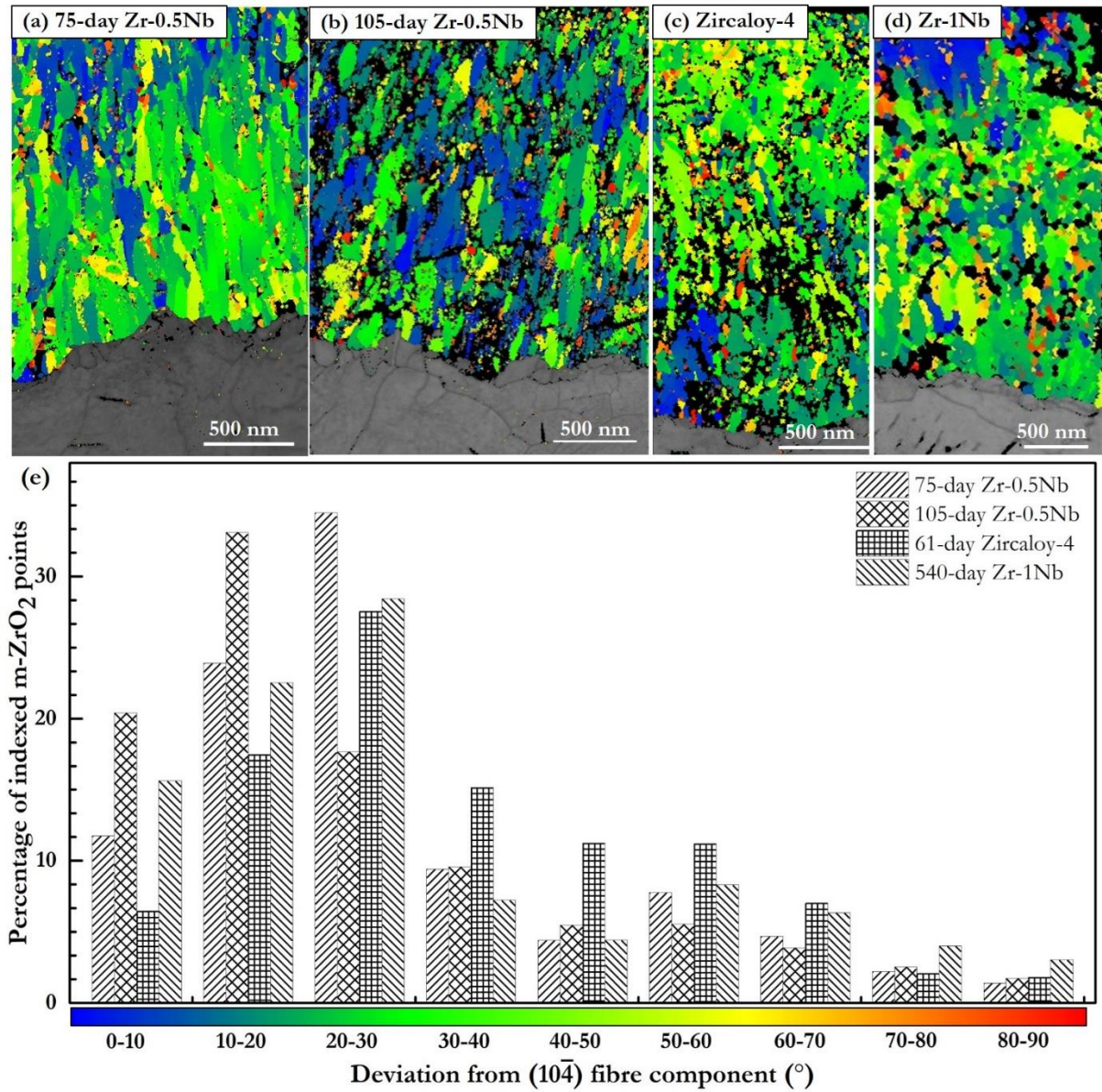


Fig. 3. Combined TKD m-ZrO<sub>2</sub> texture component and band contrast map for (a) 75-day corroded Zr-0.5Nb, (b) 105-day corroded Zr-0.5Nb, (c) 61-day corroded Zircaloy-4 and (d) 540-day corroded Zr-1Nb alloy. The grains are colored according to the angular deviation of their (104) poles from the ND. (e) Statistics showing the frequencies of grains with the (104) poles deviating with specific angular ranges away from the ND.



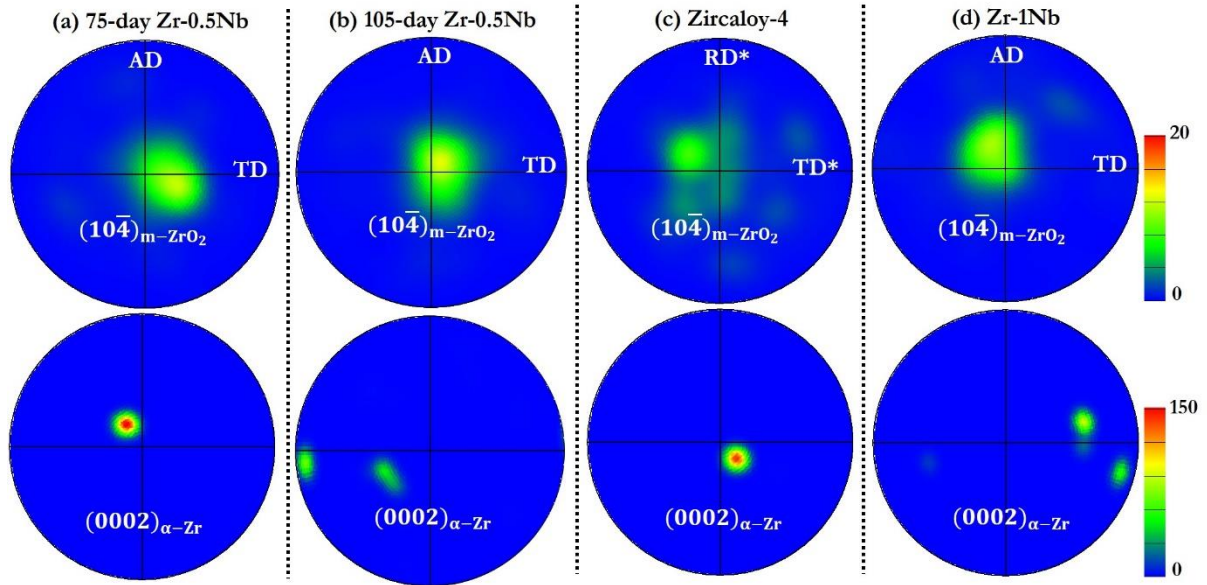


Fig. 4. Contoured  $(10\bar{4})$  poles (half width  $20^\circ$ ) of all the  $m\text{-ZrO}_2$  grains and  $(0002)$  poles (half width  $10^\circ$ ) of the underlying  $\alpha\text{-Zr}$  substrate viewed along the oxide growth direction for (a) 75-day corroded Zr-0.5Nb tube, (b) 105-day corroded Zr-0.5Nb tube, (c) Zircaloy-4 sheet and (d) Zr-1Nb tube sample. (In the tube sample AD: axial direction, TD: tangential direction; in the sheet sample RD\*: rolling direction, TD\*: transverse direction)

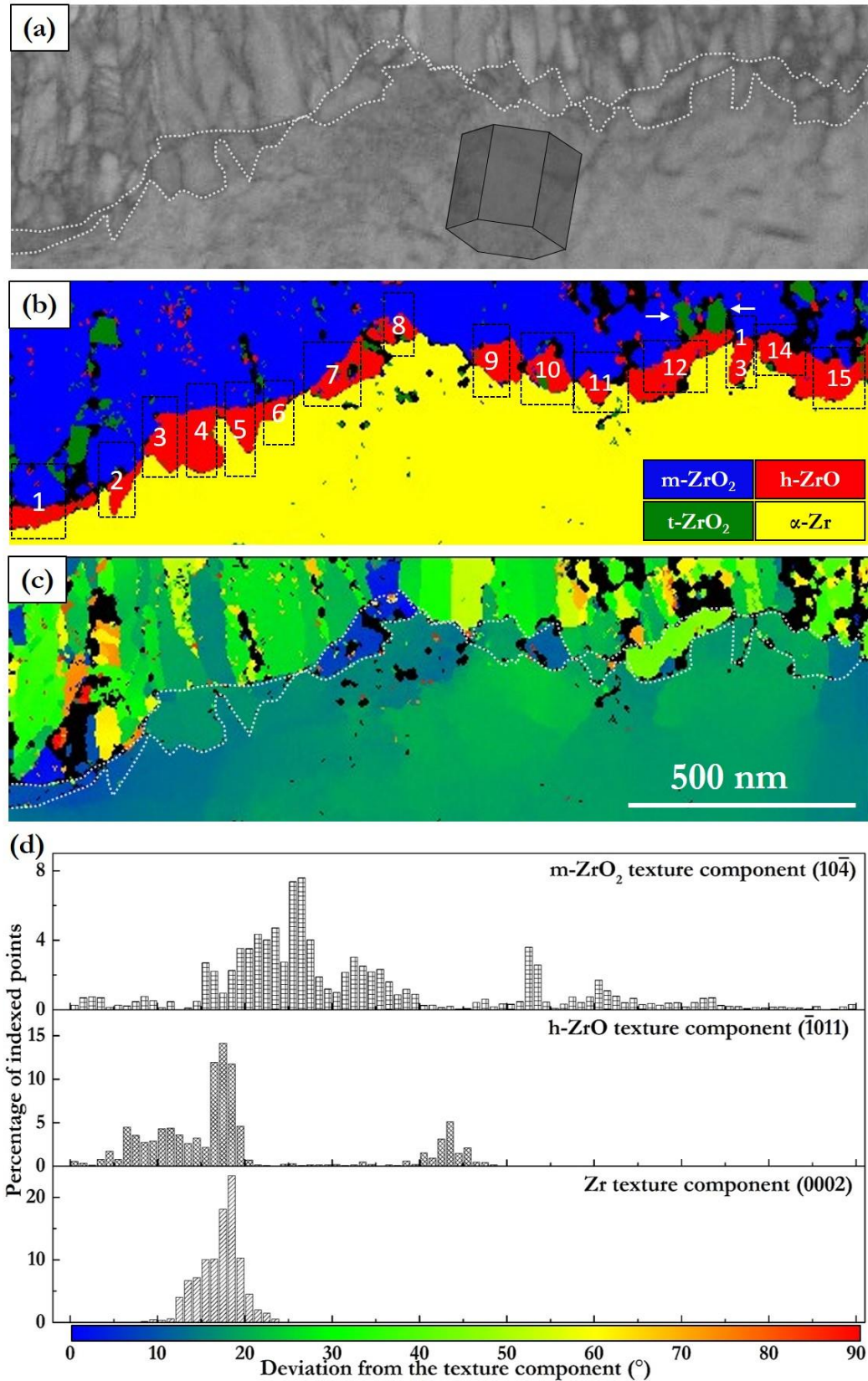


Fig. 5. Enlarged TKD maps of the oxide/metal interface region in the Zr-0.5Nb tube sample, (a) band contrast map with schematic crystalline orientation of the substrate, (b) phase map and (c) texture component maps for the m-ZrO<sub>2</sub>, h-ZrO and α-Zr. The grains are colored according to their angular deviation from the radial direction. (d) statistics and legend showing the frequencies of specific angular deviations away from the radial direction.

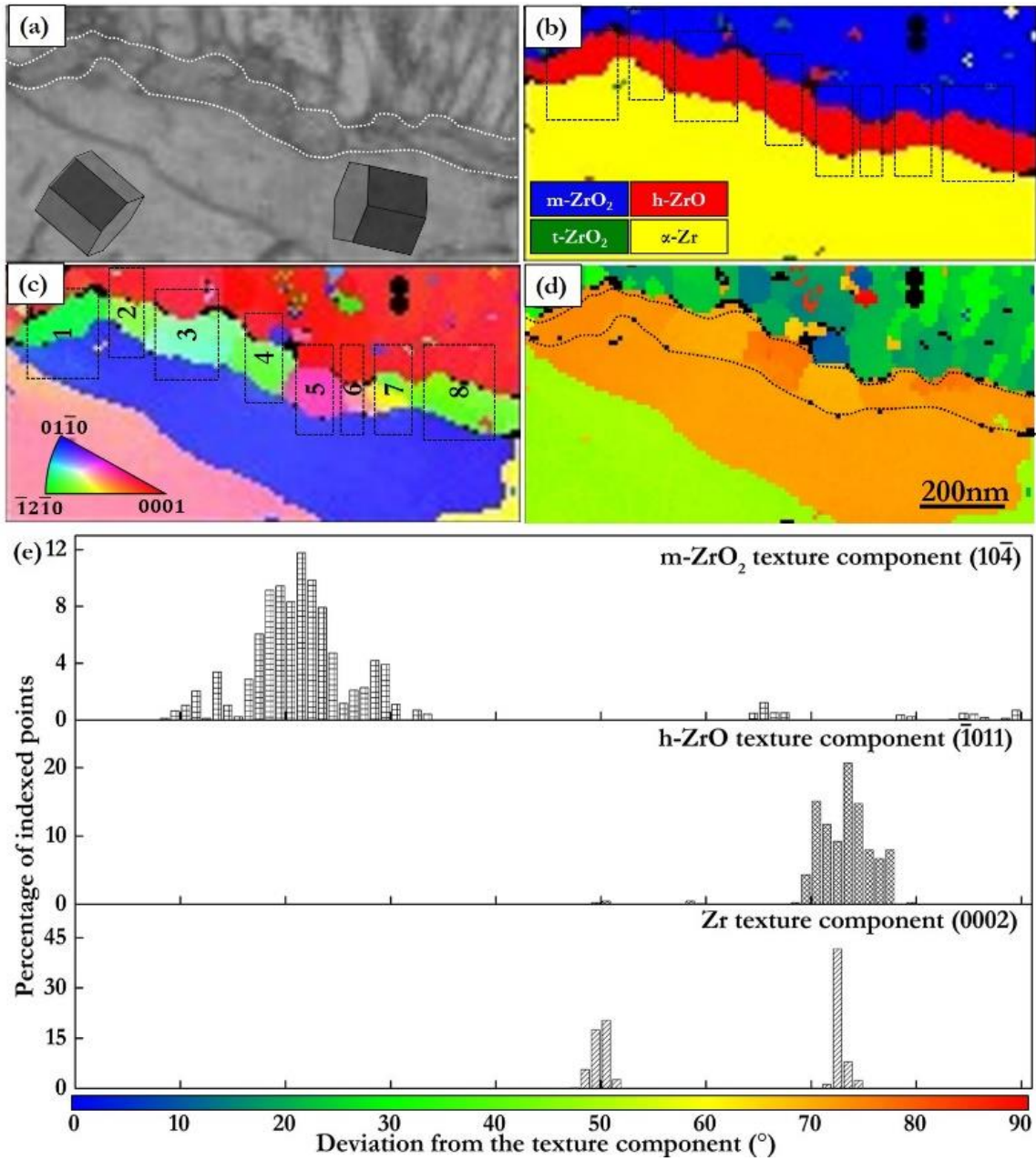


Fig. 6. Enlarged TKD maps of the oxide/metal interface region in the Zr-1Nb tube sample (a) band contrast map with schematic crystalline orientation of the substrate, (b) phase map and (c) inverse pole figure Y (IPFY) map with the corresponding legend for h-ZrO and α-Zr, (d) texture component map where the grains are colored according to their angular deviation from the radial direction shown in (e). (e) the frequencies of specific angular deviations away from the radial direction. Grain-by-grain analysis regions are identified in (b) and (c).



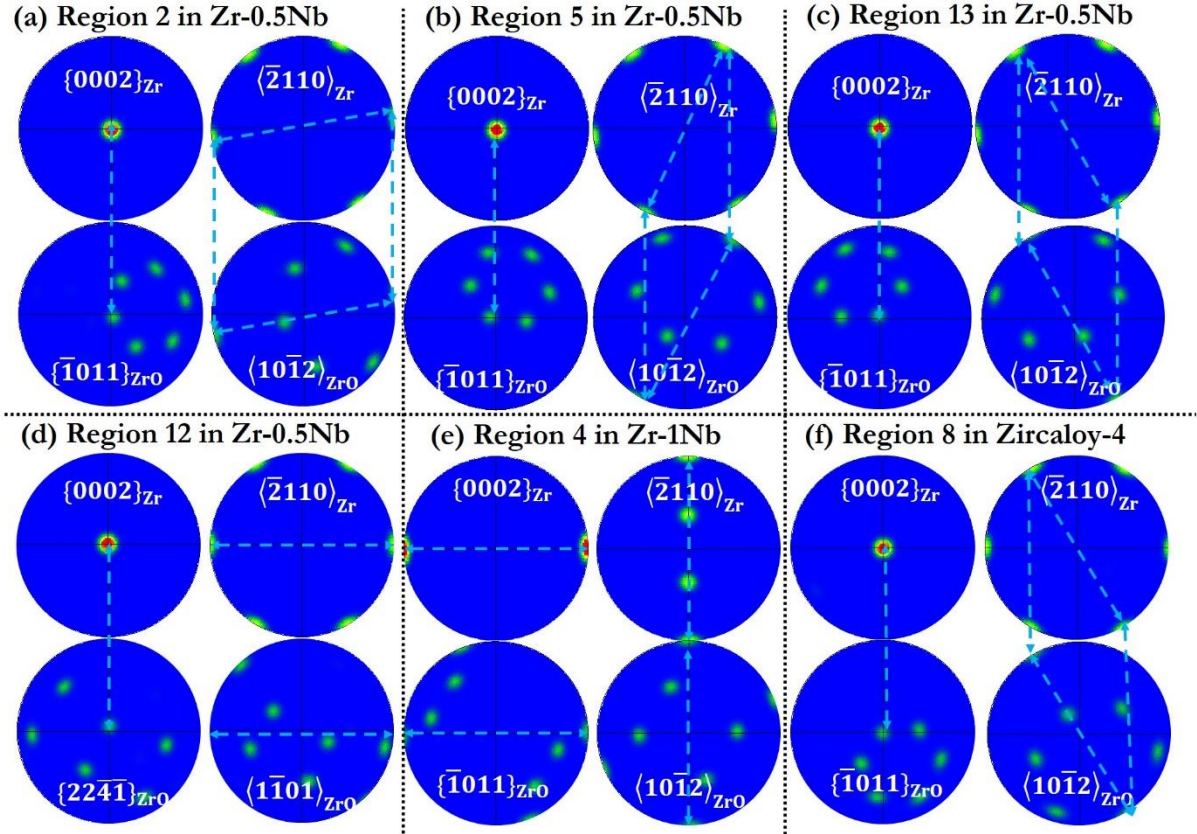


Fig. 7. Pole figures of grain-by-grain analysis showing the orientation relationships between individual h-ZrO suboxide grains and the underlying  $\alpha$ -Zr substrate in the (a, b, c and d) 75-day corroded Zr-0.5Nb, (e) 540-day corroded Zr-1Nb and (f) 61-day corroded Zircaloy-4 samples.

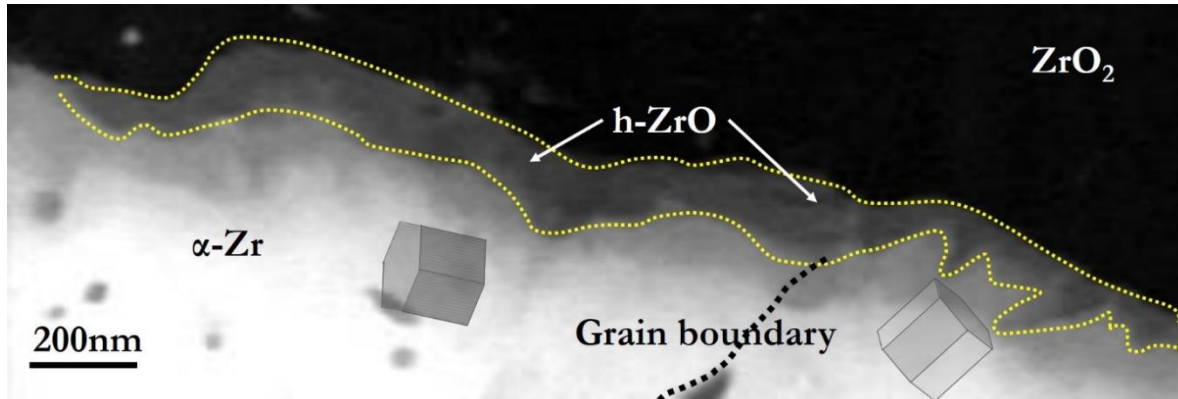


Fig. 8. MLLS Fitted EELS spectra map showing the positions of oxide, suboxide and metal substrate. Details about using EELS MLLS fitting spectra to reveal the position and morphology of the different phases at the metal/oxide interface can be found in [69, 70]. The crystalline orientations of the substrate are identified by TKD.

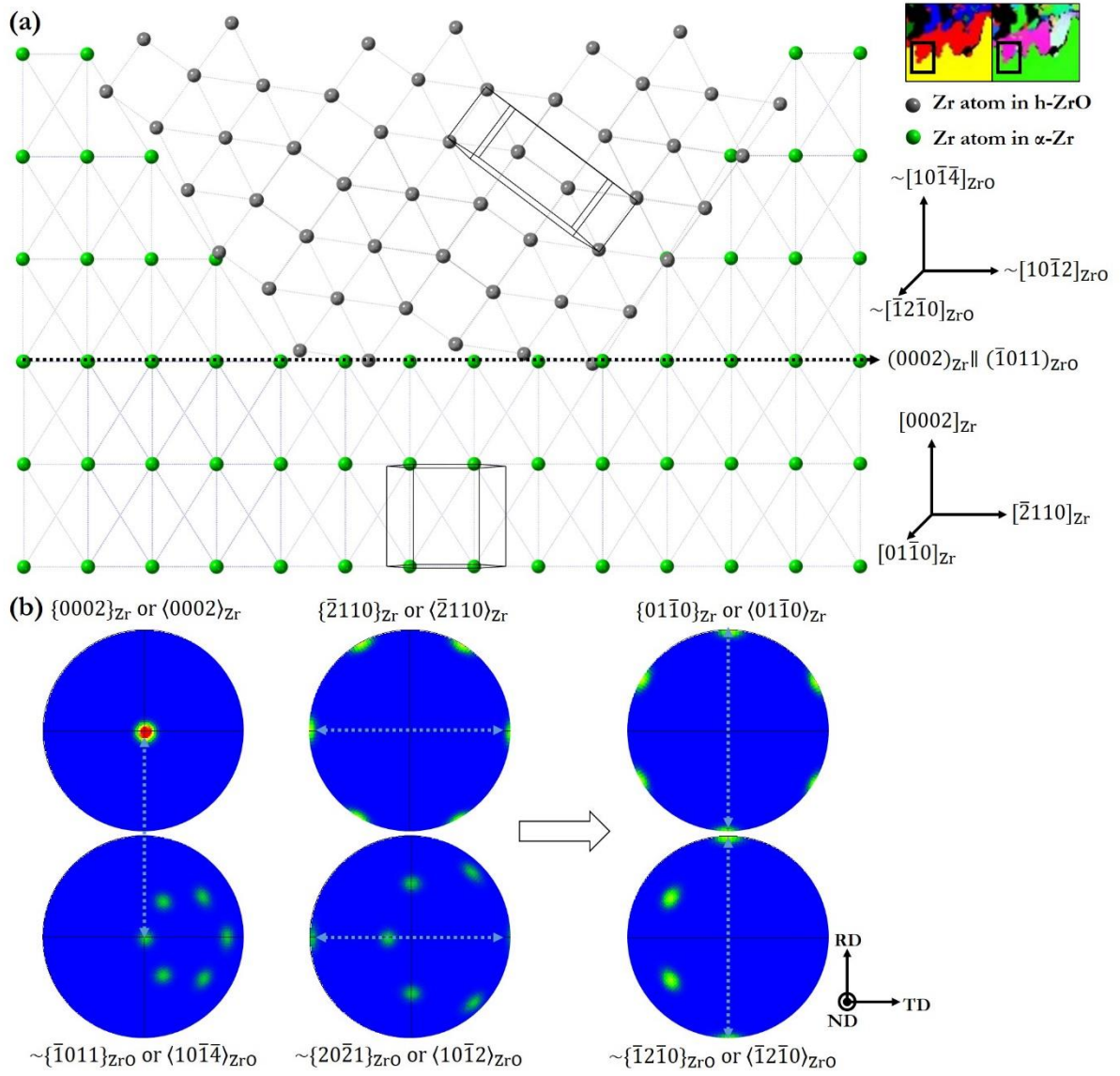


Fig. 9. (a) Reconstructed atomic arrangements (single stacking plane shown) of the h-ZrO/α-Zr interface for the Zircaloy-4 sample based on TKD phase and IPF maps. (b) pole figures of the h-ZrO suboxide and α-Zr from the region of interest. To reveal the interface atomic arrangement more clearly, we have manually adjusted the Euler angles for both phases (from  $\varphi_1=11.4^\circ$ ,  $\psi=100.5^\circ$ ,  $\varphi_2=30.7$  to  $\varphi_1=1.3^\circ$ ,  $\psi=90.7^\circ$ ,  $\varphi_2=28.7$ ) so that the underlying α-Zr grain can be orientated with (0002) in the center of the stereographic projection.



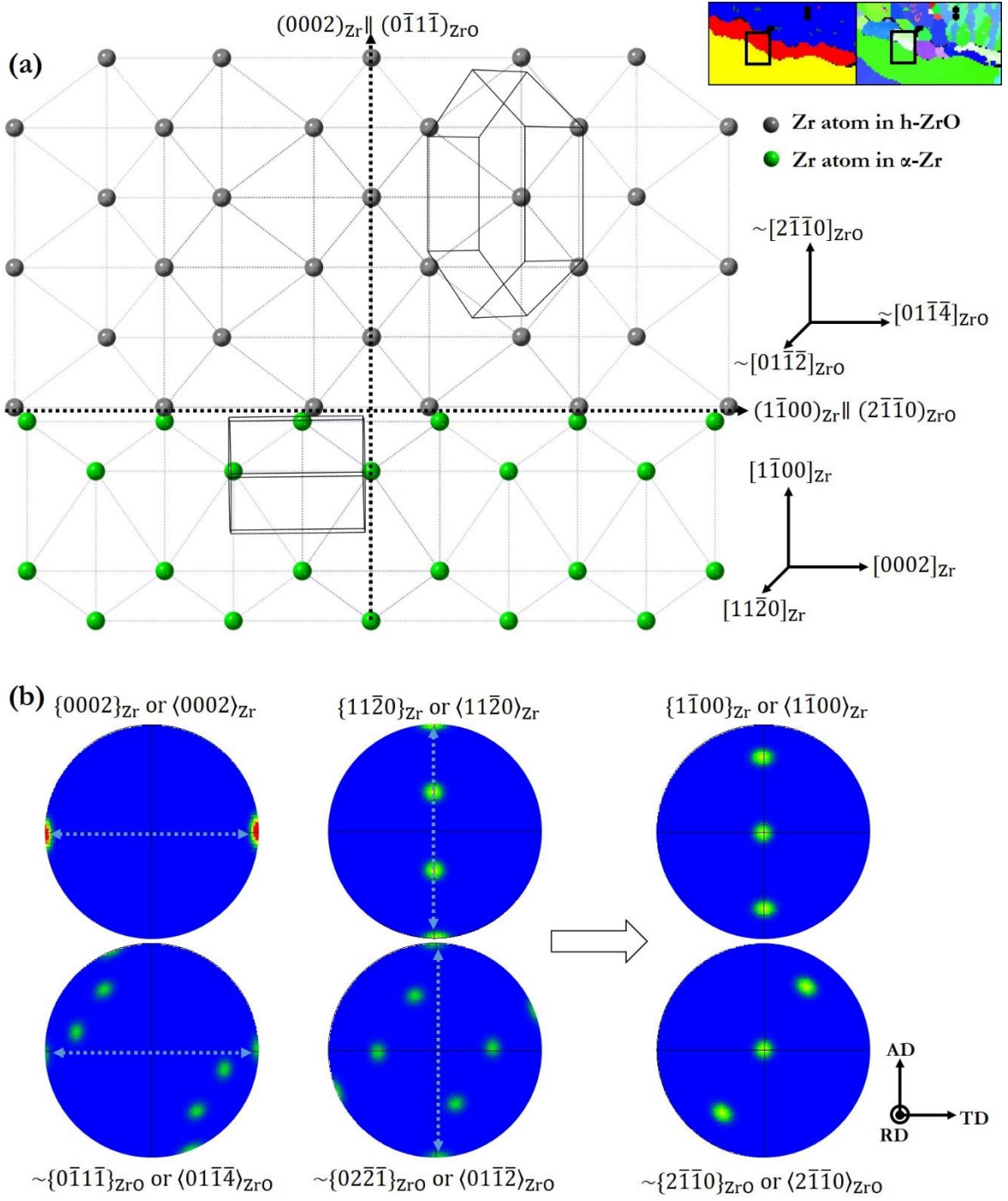


Fig. 10. (a) Reconstructed atomic arrangements (single stacking plane shown) of the h-ZrO suboxide and  $\alpha$ -Zr based on the TKD phase and IPF maps for the Zr-1Nb sample. (b) pole figures of the h-ZrO suboxide and  $\alpha$ -Zr from the region of interest. To reveal the interface atomic arrangement more clearly, we manually changed the Euler angles (from  $\varphi_1=77.8^\circ$ ,  $\psi=104.1^\circ$ ,  $\varphi_2=3^\circ$  to  $\varphi_1=89.2^\circ$ ,  $\psi=-89.6^\circ$ ,  $\varphi_2=59^\circ$ ) so that the underlying  $\alpha$ -Zr grain can be orientated with  $[0002]$  at the center of the stereographic projection.

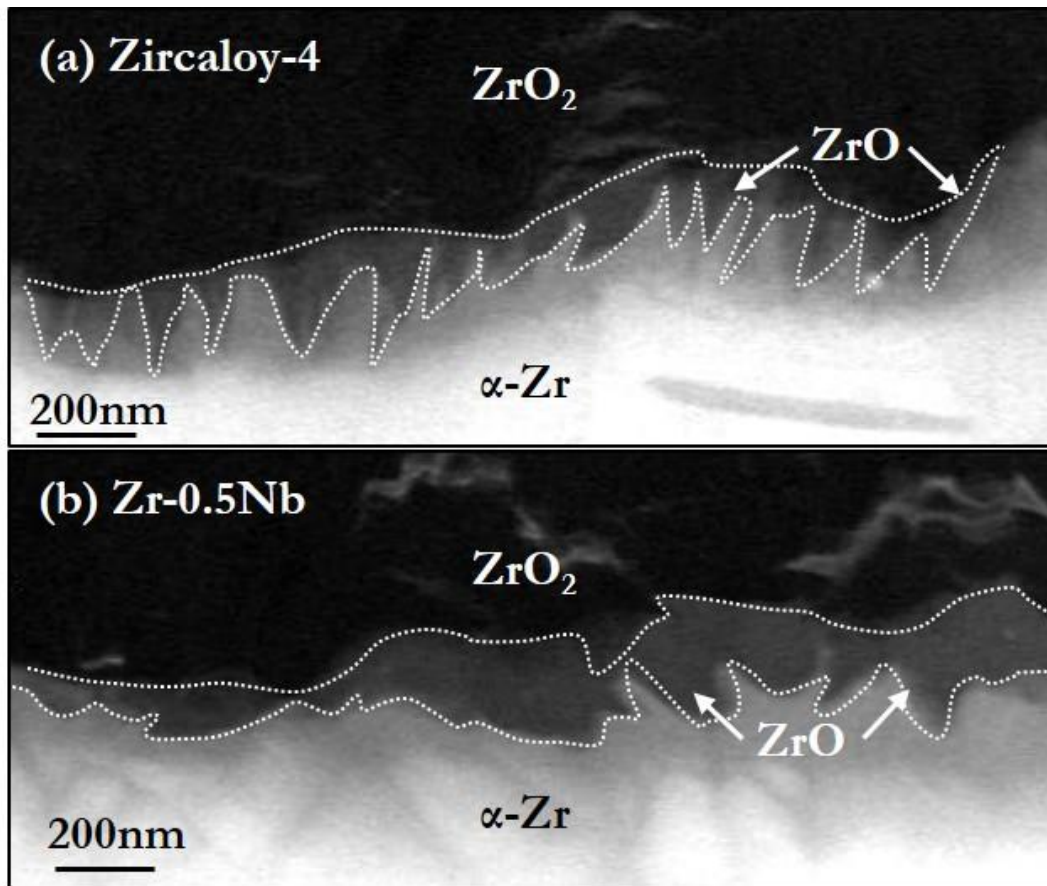


Fig. 11. MLLS Fitted EELS spectra maps showing the shape of suboxide grains in different alloys, (a) recrystallized Zircaloy-4 sheet (106 days corrosion, oxide thickness  $\sim 2.6 \mu\text{m}$ ), (b) recrystallized Zr-0.5Nb tube (105 days corrosion, oxide thickness  $\sim 2.5 \mu\text{m}$ ).

Mechanism of the  $\alpha$ -Zr to hexagonal-ZrO transformation and its impact on the corrosion performance of nuclear Zr Alloys

Junliang Liu<sup>1\*</sup>, Hongbing Yu<sup>2</sup>, Phani Karamched<sup>1</sup>, Jing Hu<sup>3</sup>, Guanze He<sup>1</sup>, Daniel Goran<sup>4</sup>, Gareth M. Hughes<sup>1</sup>, Angus J Wilkinson<sup>1</sup>, Sergio Lozano-Perez<sup>1</sup>, Chris R.M. Grovenor<sup>1</sup>

<sup>1</sup>Department of Materials, University of Oxford, Parks Road, OX1 3PH, UK

<sup>2</sup>Department of Engineering Science, University of Oxford, Parks Road, Oxford OX1 3PJ, UK

<sup>3</sup>Argonne National Laboratory, 9700 S. Cass Avenue, Argonne, IL 60439, United States

<sup>4</sup>Bruker Nano GmbH, Am Studio 2D, 12489, Berlin, Germany

\*Corresponding author: bryanchina@hotmail.com

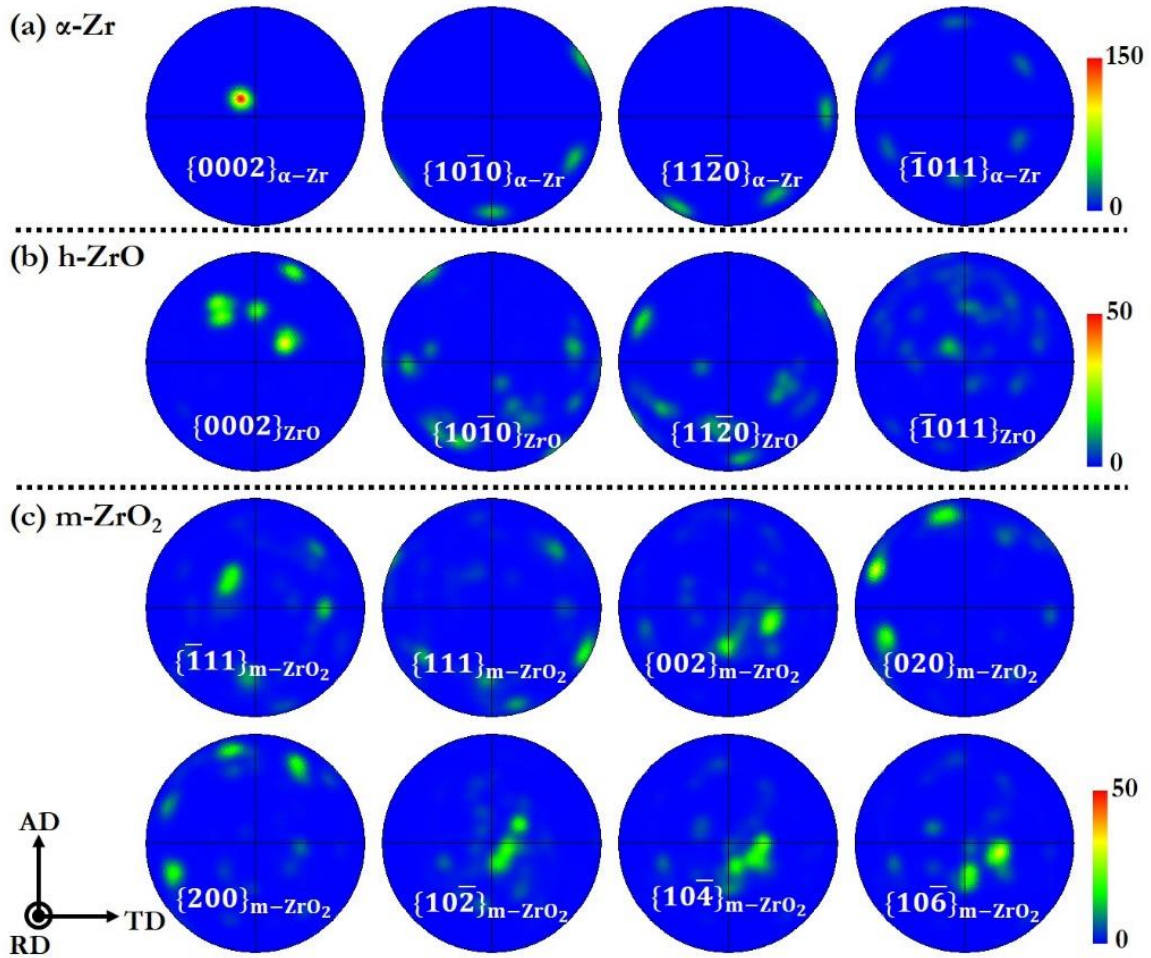


Fig. S1 Contoured distributions of low index poles (half width 10°) from the  $\alpha$ -Zr substrate, h-ZrO and adjacent m-ZrO<sub>2</sub> near the oxide/metal interface in the Zr-0.5Nb tube sample

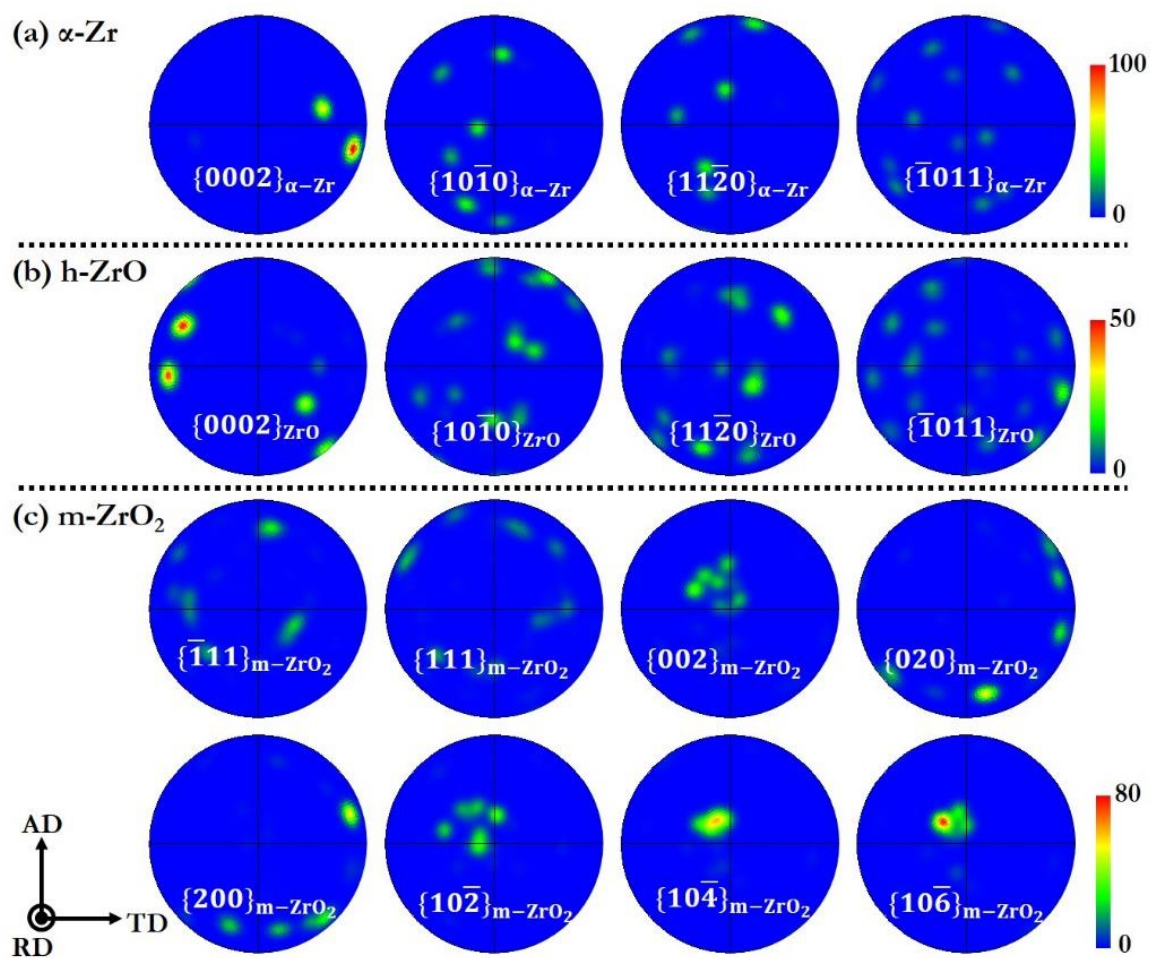


Fig. S2 Contoured distributions of low index poles (half width 10°) from the  $\alpha$ -Zr substrate, h-ZrO and adjacent m-ZrO<sub>2</sub> near the oxide/metal interface in the Zr-1Nb tube sample



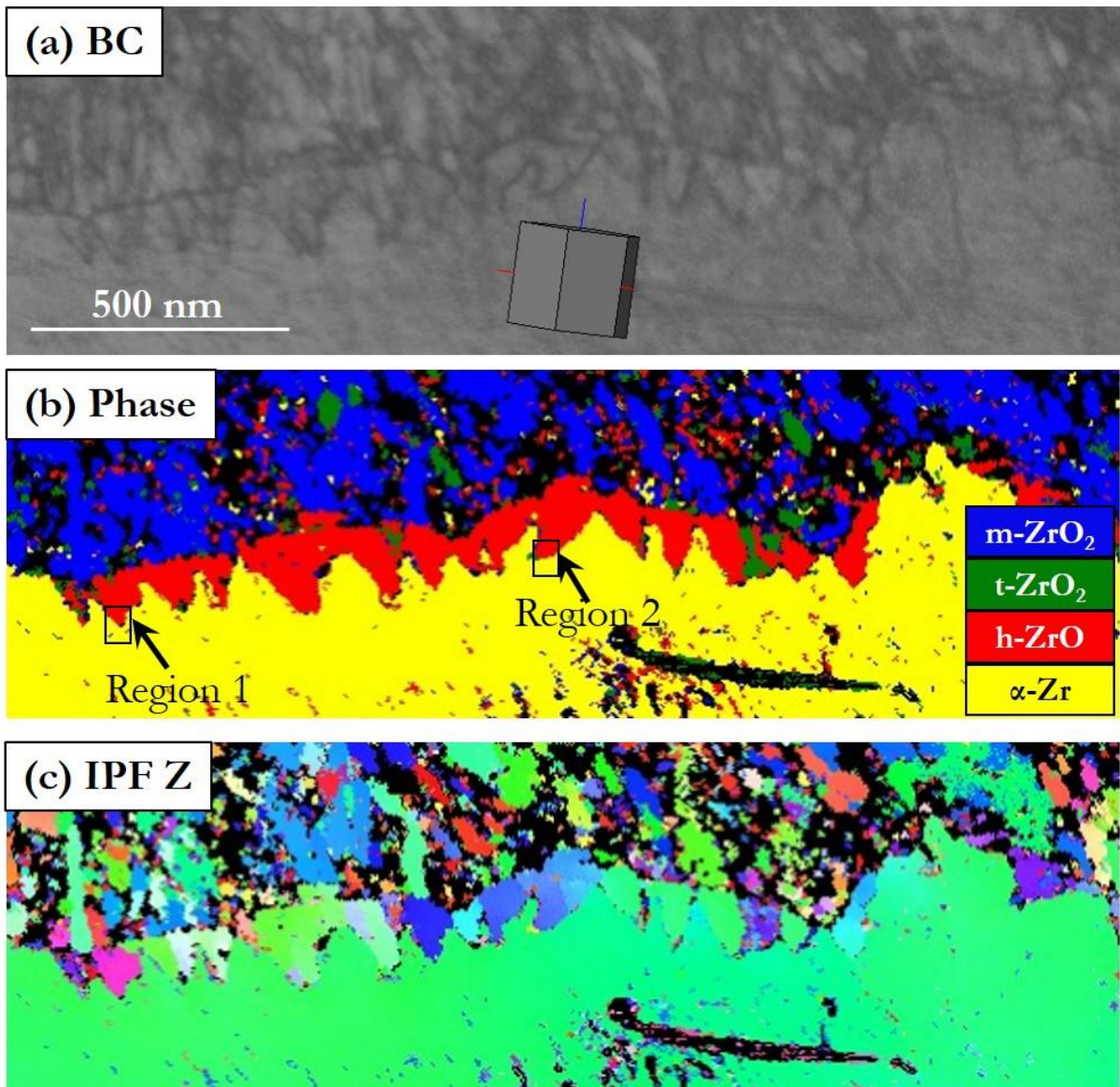


Fig. S3 TKD maps of the oxide/metal interface region in the 105-day Zircaloy-4 sample, (a) band contrast map with schematic crystalline orientation of the substrate, (b) phase map and (c) IPF orientation

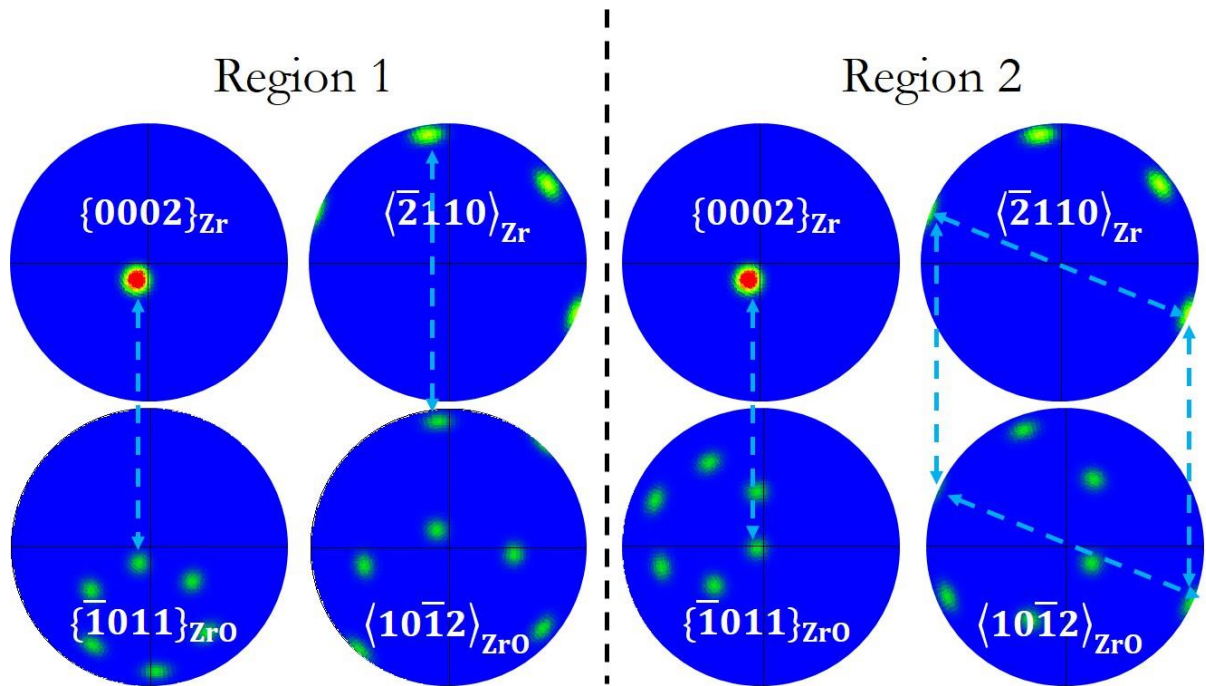


Fig. S4 Pole figures of grain-by-grain analysis showing the orientation relationships between individual h-ZrO suboxide grains (region 1 and region 2 highlighted in Fig. S4) and the underlying  $\alpha$ -Zr substrate in the 105-day corroded Zircaloy-4 sample.

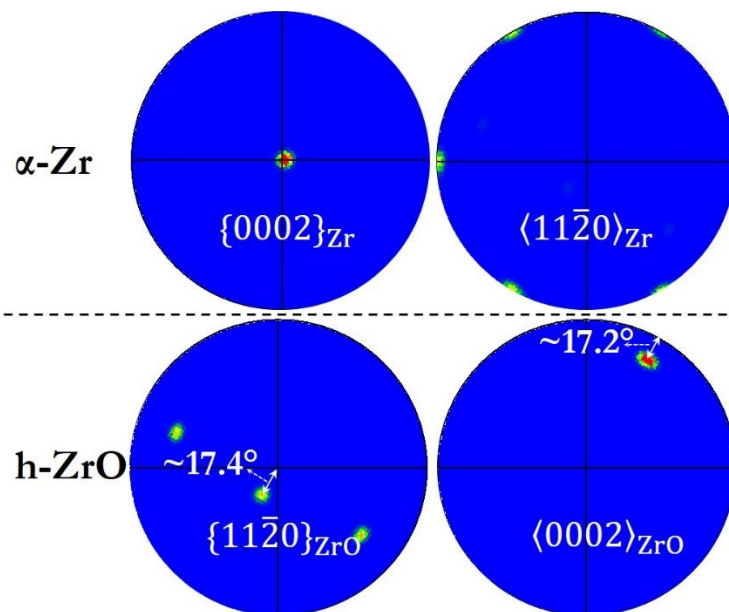


Fig. S5 Contoured distributions of poles (half width  $5^\circ$ ) compare the position of  $\{0002\}_{\text{Zr}}$ ,  $\langle 11\bar{2}0 \rangle_{\text{h-ZrO}}$  and  $\{11\bar{2}0\}_{\text{h-ZrO}}$ ,  $\langle 0002 \rangle_{\text{h-ZrO}}$  from region 12 in the Zr-0.5Nb sample. The literature [27, 35] proposed these poles are perfectly aligned.